

Chronology of southern Nicola arc stratigraphy and deformation



Mitchell G. Mihalynuk^{1, a}, Larry J. Diakow¹, Richard M. Friedman², and James M. Logan³

¹ British Columbia Geological Survey, Ministry of Energy and Mines, Victoria, BC, V8W 9N3

² Pacific Centre for Geochemical and Isotopic Research, University of British Columbia, Vancouver, BC, V6T 1Z4

³ JLoGeologic, Victoria, BC, V8L 5Z9

^a corresponding author: Mitch.Mihalynuk@gov.bc.ca

Recommended citation: Mihalynuk, M.G., Diakow, L.J., Friedman, R.M., and Logan, J.M., 2016. Chronology of southern Nicola arc stratigraphy and deformation. In: Geological Fieldwork 2015, British Columbia Ministry of Energy and Mines, British Columbia Geological Survey Paper 2016-1, pp. 31-63.

Abstract

Field observations and new isotopic age determinations from the Southern Nicola Arc Project (SNAP) necessitate further revision of the Nicola arc stratigraphy. New U-Pb CA-TIMS dates significantly extend igneous limits of the Nicola Group. Volcanic crystallization ages now range from ~238 Ma, latest Middle Triassic (Ladinian), to ~202 Ma, latest Triassic (Rhaetian). The youngest age marks the end of Nicola arc development in southern Quesnellia, culminating an interval that started in the late Norian during which volcanism was sporadic and sedimentation of arc-derived detritus was predominant. Late erosion that cuts down to early Norian carbonate rocks, combined with a predominance of mafic magmatism, might account for a lack of datable material between ~223 Ma and ~210 Ma. Resurgence in arc volcanism and eruption of the Harmon succession developed above oxidized basal conglomerate in the late Norian, after ~208 Ma. It is closely timed and possibly succeeded by emplacement of intrusions hosting Cu-Au porphyry mineralization, but also by denudation of the Nicola magmatic arc and accumulation of volcanic and plutonic detritus. A period of Early Jurassic plutonism separates the Nicola Group from a newly defined ~162 Ma volcanic succession, to our knowledge the first to be documented in south-central British Columbia. Named the Osprey unit, and composed of rhyolite and andesite volcanic rocks, they are cut by the nearly coeval and presumably comagmatic Osprey batholith.

The Nicola arc strata were deformed at least three times. First, thick beds of maroon conglomerate containing clasts derived from Nicola arc strata as young as Norian (~210 Ma) were deposited between 208 and 201 Ma in the central part of the study area, coeval with fine-grained deposits to the east, presumably recording uplift. Variable magmatism ranges from strongly alkalic basalts to calc alkaline apatite-biotite-quartz-phyric pyroclastic strata (~202 Ma) with associated copper mineralization. Second, we speculate that Nicola strata were folded and thrust and overlain by conglomeratic strata (Shea conglomerate). Detrital zircon ages from the conglomerate and youngest underlying strata indicate that this deformation was between 201 and 185 Ma, when Quesnel terrane was docking at the margin of North America. Third, thrust-imbriation of chert pebble conglomerate and Nicola Group strata is constrained by detrital zircon ages from the conglomerate and by crystallization ages from undeformed Spences Bridge Group volcanic strata to between ~134 and 104 Ma, possibly related to docking of the Insular Superterrane.

Keywords: Stratigraphy, geochronology, Nicola Group, Nicola arc, porphyry copper gold, Princeton, Merritt, Spences Bridge Group, Quesnel terrane, Intermontane Superterrane, subduction, collision, deformation, biogeochronology, paleogeography

1. Introduction

Late Triassic porphyry deposits are well known in the conjoined Stikine and Quesnel terranes, which comprise most of the accreted crust along the length of British Columbia (Fig. 1). Prolific porphyry mineralization at 205 ±6 Ma produced >90% of the known copper resource in these terranes (Logan and Mihalynuk, 2014). Owing in part to its spectacular metal endowment, the southern Nicola arc in Quesnel terrane has been extensively explored (reviews of exploration can be found in Preto, 1979; Mihalynuk and Logan, 2013b; Mihalynuk et al., 2014a, 2015; and references therein). Since 2012, fieldwork of the Southern Nicola Arc Project (SNAP) has built upon this body of knowledge, particularly between the producing deposits at Copper Mountain (south), Highland Valley (northwest) and Iron Mask (Afton, northeast; Fig. 1). Geochronologic studies at each of these deposits have defined the age of mineralization at ~204 Ma (Mihalynuk et al., 2010; Ash et al., 2007; Logan

et al., 2007, although the apparent mineralizing phase of the Guichon batholith at the Highland Valley deposit (Bethsaida phase) has returned older ages of ~209 Ma, Davis in Logan and Mihalynuk, 2014).

Magmatic and sedimentary units of the southern Nicola arc have been classically thought of as forming three subparallel belts separated by northerly trending faults: the Western belt distinguished by felsic volcanic rocks and limestone; the Central belt with mainly mafic volcanic rocks, comagmatic plutons, and locally prominent coarse siliciclastic rocks; and the Eastern belt containing the highest proportion of sedimentary rocks (Preto, 1979, and extended more regionally by Monger, 1989; Figs. 2, 3). All were thought to be strictly Late Triassic and relatively unaffected by contractional deformation. Using isotopic dating techniques unavailable to earlier workers, our work has shown that initial growth of the southern Nicola arc started in the Middle Triassic and continued episodically to latest Triassic,

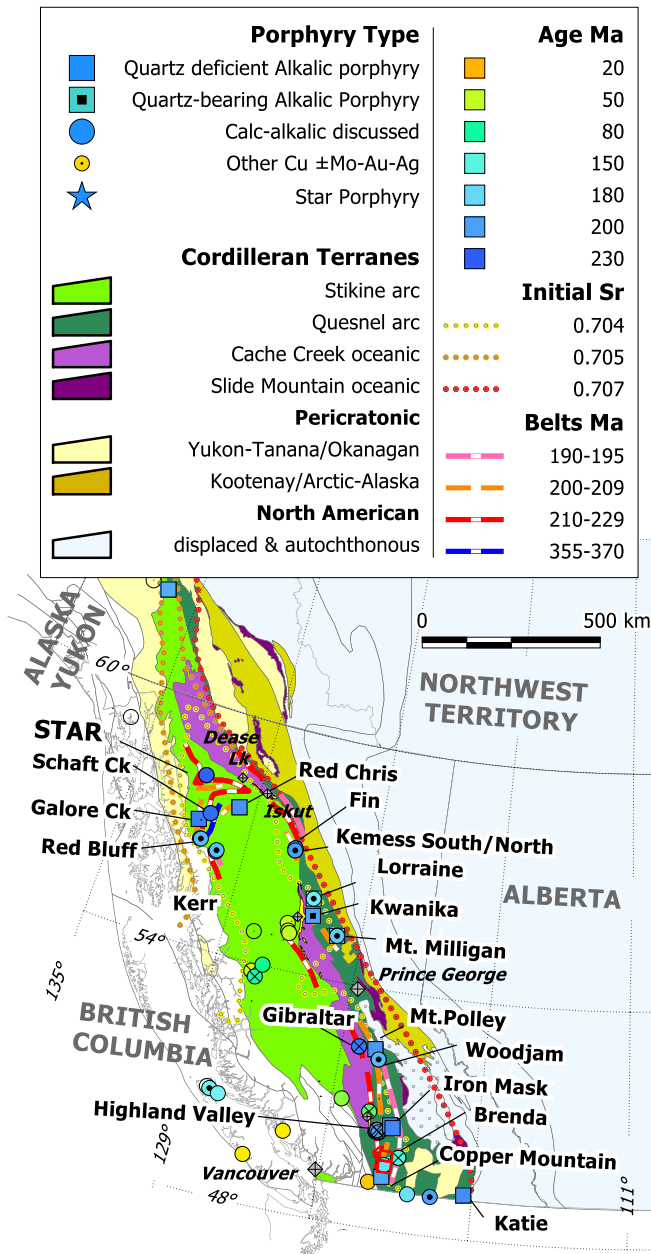


Fig. 1. Tectonostratigraphic terranes of interior British Columbia and major porphyry Cu-Au deposits (modified after Logan and Mihalynuk, 2014). Porphyry deposits are colour coded according to age to show Late Triassic-Early Jurassic porphyry events (shades of blue). Red outline between Copper Mountain and Iron Mask corresponds to the study area outlined in Figure 2.

and that late shortening, affected the entire arc (Mihalynuk et al., 2015). Recent U-Pb zircon data now extend the age and distribution of Nicola magmatism, with felsic pulses at ~238 Ma and ~202 Ma in the Central belt, and ~239 and ~224 Ma in the Western belt (Figs. 2, 3). The youngest detrital zircons from maroon sandstones in the Central belt (Harmon succession) yielded ages of ~208 to 204 Ma (Mihalynuk et al., 2015) consistent with the magmatic ages suggesting that Nicola arc

magmatism ceased near the Triassic-Jurassic boundary (~201 Ma; Cohen et al., 2015).

Herein we summarize the results of 15 new isotopic age determinations (see Friedman et al., 2016 for details), and focus on the stratigraphic revisions they necessitate. In some instances, the new data lead to significant revisions of the age relationships in the Central and Eastern belts that were inferred by Mihalynuk et al. (2014, 2015). For example, although Mihalynuk et al. (2015) acknowledged interfingering of volcanic and sedimentary strata in the Eastern belt, they considered that the main sedimentary succession served as basement to the arc. As shown below, the youngest detrital zircon ages require that at least the western exposures of the Eastern belt are coeval with youngest arc magmatism (~202 Ma) and hence the notion of an arc constructed above thick turbiditic deposits remains unsubstantiated. Knowledge of the timing, style, and magnitude of folding and faulting is key to discovering the offset parts of known deposits such as the Boundary fault, which truncates mineralization in the Copper Mountain deposit (Preto, 1972). We also focus in this paper on using the new ages to further refine the chronology of deformation in the mineralized arc.

2. Regional geology

Most rocks of the southern Nicola arc in the study area belong to more than a dozen lithostratigraphic units that can be traced for many kilometres along the arc, and in some cases, across the arc, in either the Central or Eastern belts. Plutons and stocks of various ages have traditionally provided relative age brackets for these units, augmented by relatively few fossil ages from sedimentary units. More detailed descriptions of these units than provided below can be found in the pioneering work of Preto (1979) and in Mihalynuk et al. (2014a, 2015). Readers seeking more regional lithologic information are directed to Monger (1984). Lithologic descriptions herein focus primarily on the Western belt.

2.1. Triassic layered rocks, Eastern and Central belts

The distribution and age relationships of Triassic units in the Eastern and Central belts along a transect at the latitude of ~50°N are presented in Figure 3. Abrupt and non-systematic changes of unit ages in laterally adjacent parts of the transect reflect levels of exposure, largely a consequence of faults. The transect crosses, from east to west (red boxes Fig. 3): 1) the Eastern sedimentary belt, containing mainly well-bedded siltstone and sandstone (<210 Ma in part, this paper); 2) the Paradise succession of polymictic conglomerate with volcanic (and commonly abundant monzonitic) clasts, and including the Boot Lake subdivision, with mainly coarse augite- and hornblende-phyric clasts; 3) the Shrimpton succession of massively-bedded, coarse feldspathic wacke and tuffaceous rocks, calcareous argillaceous volcanic siltstone, limestone-clast bearing conglomerate, and analcime-rich flows; 4) coarse augite porphyry breccia (commonly reworked) and rare flows; 5) Ketcham rhyolite clast sharpstone conglomerate and quartz-

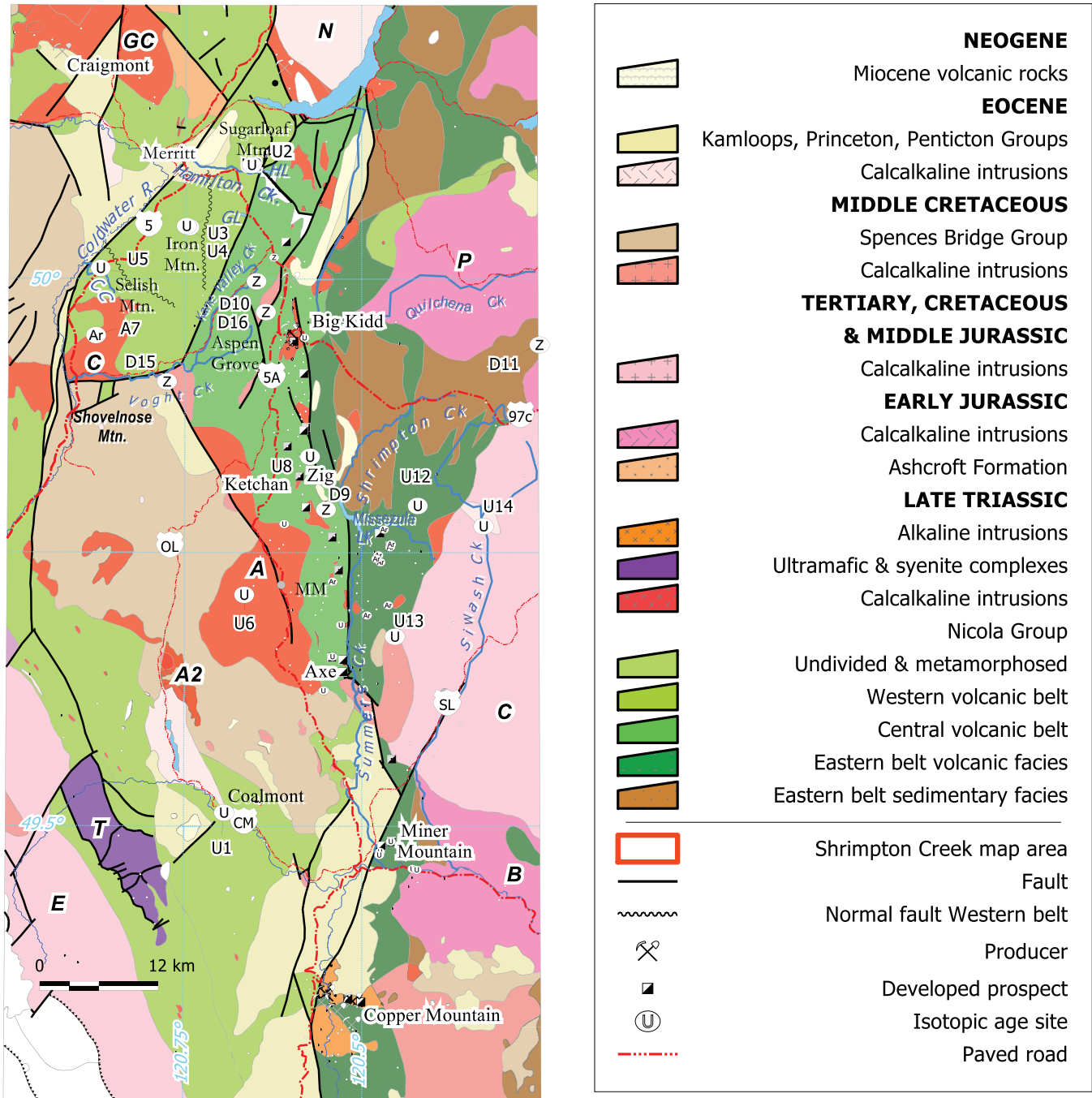


Fig. 2. Geological setting of field mapping and geochronology samples presented in this report. Extents of Preto's (1979) Eastern belt (mafic submarine volcanic and sedimentary rocks), Central belt (arc axis, mafic volcanic and coeval intrusive rocks) and Western belt (intermediate to felsic volcanic and sedimentary rocks) are shown for reference, after Massey et al. (2005); modified from Mihalynuk and Logan (2013b). Abbreviations for major plutons: A = Allison Lake, A2 = newly mapped southwest extension of the Allison pluton, B = Bromley, BI = Boulder intrusion, E = Eagle, GC = Guichon Creek, MM = Missequela Mountain, N = Nicola, O = Osprey Lake, P = Pennask, S = Summers Creek, T = Tulameen complex. See Figure 1 for context. Orange box = 2013 mapping, red box = 2014 mapping, yellow outline = 2015 mapping and Diakow and Barrios (2008). Labels beside geochronologic sampling sites correspond to those in Figure 3 and Table 1. Small isotopic age site symbols are from previously published data.

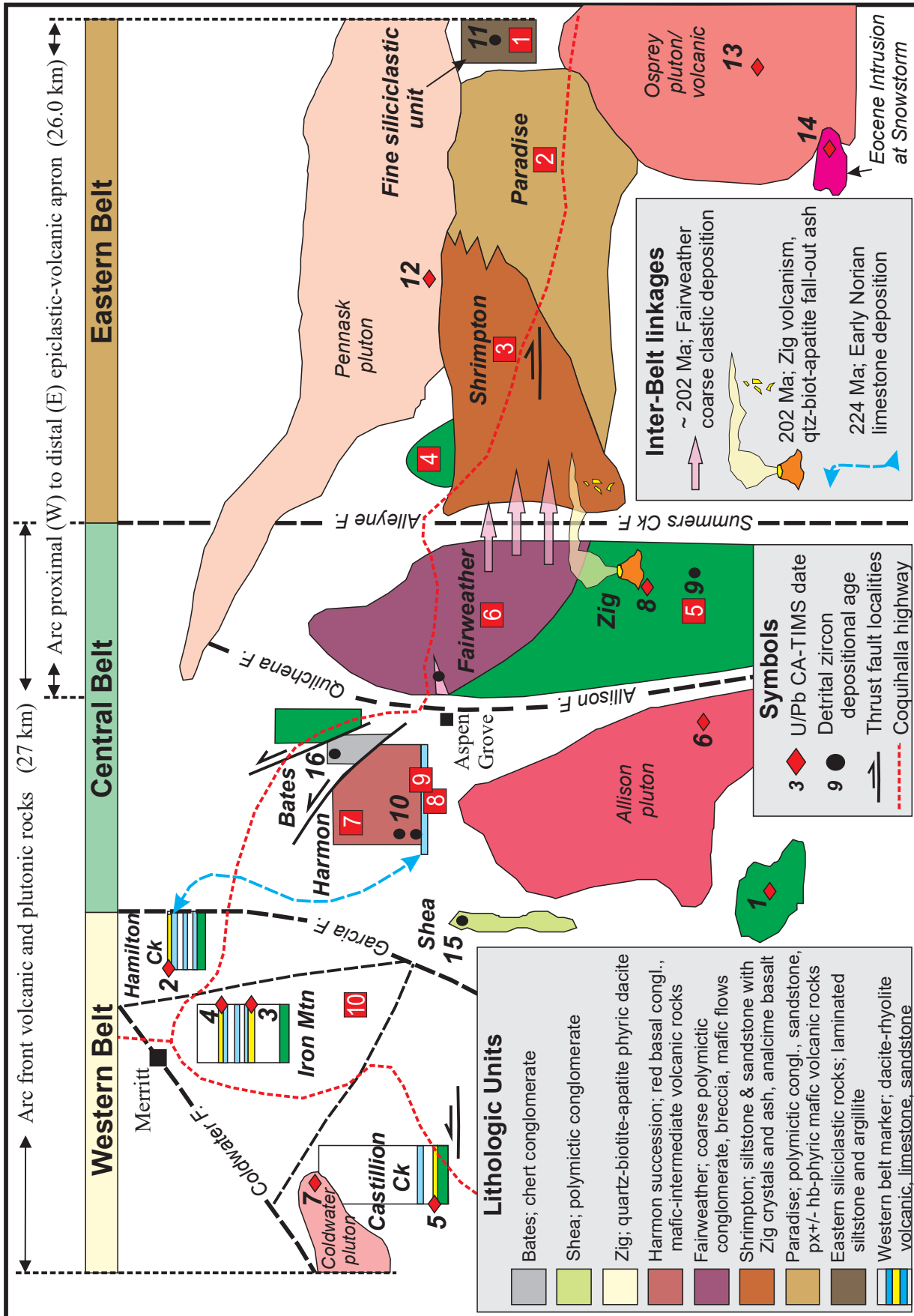


Fig. 3. Schematic diagram showing the general distribution of the Nicola Group at the latitude of ~50°N (Coquihalla Highway 5 and 97C) near Merritt, which transects mainly volcanic rocks in the Western and Central belts, and largely siliciclastic rocks that pass from the Central belt into the Eastern belt. Dated units demonstrate temporal continuity between the Nicola belts. Ages are identified by bold black numbers cross-referenced to Table 1. Red squares represent areas 1-10 referred to in text.

rich sandstone (≤ 239 Ma, this study); 6) the Fairweather unit of coarse-grained siliciclastic rocks (Lefebvre, 1976), which contains Zig apatite-, biotite-, and sparse quartz-phyric tuffaceous rocks (~ 202 Ma this study) with 215 Ma calcite-quartz-epidote-chalcocite veins (Re-Os chalcocite; R.A. Creaser, unpublished); 7) bladed feldspar porphyry flows that are intercalated with maroon volcanic sandstone to aphanitic tuff, and rare cherty limestone beds (Voght unit of Harmon succession) and overlie volcanic clast-bearing conglomerate (< 210 Ma, this study) and coarse augite porphyry breccia; all overlain by feldspar porphyry volcanic breccia to ash fall tuff (Tillery unit, < 201 Ma, possibly Early Jurassic Mihalynuk et al., 2015; see below); 8) the Hendriks fossiliferous limestone and fine-grained calcareous siliciclastic beds, early Norian (~ 224 Ma; Diakow, Friedman and Orchard, unpublished fossil data; Monger, 1989); 9) Aphanitic green finely vesicular basalt interdigitated with upper parts of the Hendriks limestone; 10) Western belt felsic volcanic facies (224 Ma, this study) and siliciclastic facies (Carnian to Early Norian) which are described in more detail below.

2.2. Triassic layered rocks, Western belt

Western belt strata are separated from the Central belt by the Garcia fault, trending northeast between Garcia and Hamilton lakes (Fig. 2), and also form a fault-bounded wedge southwest of Aspen Grove (Preto, 1979). Rocks of the belt extend continuously from Hamilton Creek southwest, for 20 km to Selish Mountain where the Coldwater pluton cuts and terminates bedded strata presumed to be a younger part of the Western belt (Diakow and Barrios, 2008). The tract is about 9 km wide, bound in part or wholly by inferred faults; the Coldwater fault (Eocene) to the northwest and the Garcia fault to the southeast, which was mapped in the Hamilton Creek area (Preto, 1979), and projected southwest (Monger, 1989). Homoclinal stratified rocks throughout the tract dip moderately southeast.

Crudely bedded mafic flows and lesser volcanoclastic rocks of undetermined thickness are at the base of the homocline. Everywhere, these basalts and andesites (lower mafic unit) are overlain by a variety of bedded sedimentary and volcanic rocks (upper stratified unit). In this upper stratified unit are distinctive micritic limestones and dacite to rhyolite volcanic rocks which, recognized throughout the homocline, constitute a marker unit.

Several high-angle faults striking north and west-northwest subdivide the homocline into three major blocks. Clear offset of the lower mafic and upper stratified units show successive up-to-the-north motion resulting in deeper levels of exposure northward. In the northern block, mainly the lower mafic unit is exposed and the upper stratified unit is comparatively thin (400 m), as it increases southward to 1100 m in the central block and 1600 m in the southern block.

2.2.1. Western belt rocks at Hamilton Creek

The upper stratified unit forms a narrow band, faulted against rocks of the Central belt (Preto, 1979). Upper stratified rock

units extend discontinuously northward for at least 7 km from Garcia Lake to north of Hamilton Creek (west of Sugarloaf Mountain) where they are about 400 metres thick. In this section, grey limestone forms a series of low-lying ridges, some up to 50 metres wide. Medium to coarse feldspathic wacke and granule conglomerate, and minor basaltic flows occupy recessive areas between resistant limestone ridges. Dacitic, quartz-phyric lapilli tuffs crop out in layers several metres thick at the top of the limestone sections. Nearer Garcia Lake, these tuffs alternate with thicker limestone beds in intervals up to 25 metres thick.

Massive, crudely-layered purplish oxidized and epidote-altered dark green lava flows typify the mafic unit in the Western belt, and are extensive throughout the north block. They contain medium-grained plagioclase and augite phenocrysts and are interlayered with mafic tuff containing dark, aphanitic, indistinct fragments. The contact with the overlying stratified unit is gradational.

2.2.2. Western belt rocks at Iron Mountain

In the central block, the upper stratified unit of the Western belt may be as thick as 1100 m, as estimated from a transect originating at the crest of Iron Mountain that passes through semi-continuous exposures (see Nicola Group Iron Mountain Inset Map in Diakow and Barrios, 2008). The lithologic variability of the marker unit, which starts about 500 m above the base of the upper stratified unit, is well displayed on the southeast-facing slope of Iron Mountain (Fig. 4).

Mafic to intermediate massive flows and fragmental rocks of the lower mafic unit are predominant on the northwest slope of Iron Mountain. At the crest of the mountain, these strata are abruptly overlain by the upper stratified unit, with basal

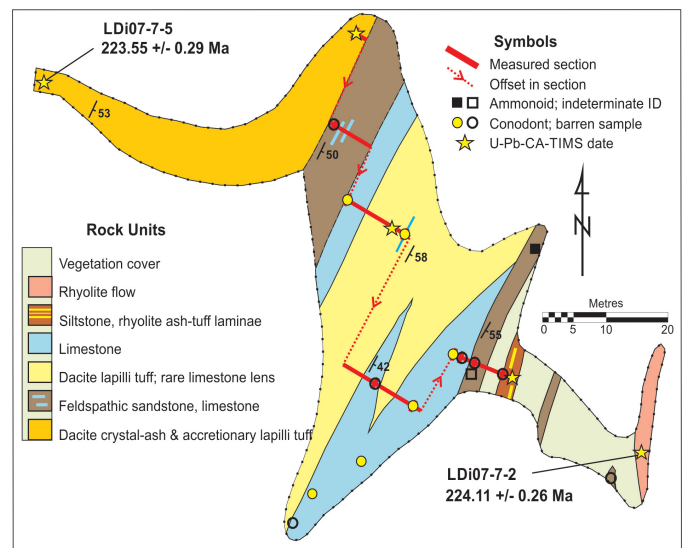


Fig. 4. Geology of the marker interval in the upper stratified unit at Iron Mountain, Western belt of the Nicola Group. Locations of samples reported herein are shown: U-Pb TIMS ages (stars) and fossil collections: conodonts (circles); ammonoids (squares). Results from other samples labelled will be presented in a future publication.

strata consisting of a dense rhyodacite flow lense, 200 to 250 m thick. These flows are overlain by a comparable thicknesses of felsic tuffs, distinguished by common aphanitic rhyolite lapilli and quartz grains, and thin layers of crystal-ash tuff. Multiple layers of accretionary lapilli tuff up to 50 cm thick are in the upper 60 metres of this felsic tuff member. These accretionary lapilli-bearing beds form the lower volcanogenic component of the marker interval (200 m thick; Fig. 4). Marker strata extend upwards for an additional 140 m through a series of limestones up to 3 m thick, and interbedded feldspathic wacke with thin lenses of carbonate and dacitic lapilli tuff. The top of the marker interval is arbitrarily set at a sharp contact with an overlying rhyolite flow unit about 40 m thick. This rhyolite in turn is overlain by a varied sequence including (from base to top): a resistant ridge-forming monolithic andesite breccia overlain by andesite porphyry flows (aggregate thickness to 200 m); maroon oxidized lapilli tuff and interlayered polymictic volcanic clast-bearing conglomerate (175 to 225 m thick), and pink-weathering limestone (10 to 30 m thick). Above this limestone, rock exposure diminishes into isolated occurrences of fine-grained quartz-bearing dacitic tuffs considered the uppermost rock unit of the central block.

2.2.3. Western belt rocks at Castillion Creek

In the south block, the upper stratified unit might be as thick as 1600 m, estimated from a transect that starts at the marker interval along the Coquihalla Highway at Castillion Creek, passing southeast, upslope through isolated exposures to Selish Mountain, then downslope through semi-continuous exposures, ending at the hydro-electric powerline corridor (Diakow and Barrios, 2008).

The marker unit at Castillion Creek is similar to that at Iron Mountain, but with several notable differences. At Castillion Creek, the marker is about 140 m thick and generally contains fewer and thinner volcanic and limestone layers, and more feldspathic wacke than at Iron Mountain. Unique to the Castillion Creek area, are stratiform siliceous beds, which occur in the mafic unit and the marker interval.

Augite-phyric mafic flows typical of the mafic unit extend upward into the lower part of the marker, interleaving with sedimentary rocks. The sedimentary rocks consist mainly of siltstone and sandstone containing angular plagioclase grains and conglomerate interbeds containing abundant angular felsic volcanic pebbles. These clastic beds typically are less than 30 cm thick, in intervals up to 12 metres thick. Carbonate rocks are scarce, comprising two units at different stratigraphic levels. The lower micritic limestone, 1.5 m thick, separates welded felsic vitric tuff layers at the base of the marker. It is grey to grey-black, with argillaceous parting between medium thick beds. More than 100 m upsection, the upper limestone overlies a second felsic pyroclastic unit. This limestone (20 m thick) is dirty grey to light grey, recrystallized and contains abundant shelly fossils.

The felsic rocks comprise sparse, relatively thin, widely spaced pyroclastic layers. The lowest layer consists of tuff

in direct contact with underlying mafic lavas; the second is 1.5 m higher, separated by limestone (Fig. 5). These vitric tuffs, each less than 30 cm thick, exhibit a welded fabric. Farther upsection, but within 12 m of the marker's base, ash-tuff occurs as parallel thin beds and laminations in feldspathic sandstone, which alternate regularly between grey, siliceous beds. Felsic tuffs recur near the middle of the marker beneath limestone beds. This upper tuff unit is 25 m thick and contains angular rhyolitic lapilli-sized fragments in a green matrix with broken plagioclase crystals. In this tuff, zones with flattened and aligned lithic fragments define a weak welded fabric suggesting deposition as a subaerial ash-flow. A rhyolite flow unit that displays fine parallel flow laminations crops out at the same elevation as the base of the Castillion marker apparently deposited on the lower mafic flow unit.

Three stratiform siliceous occurrences are widely separated within a vertically aligned, crudely stacked sequence spanning nearly a 100 m change in elevation. Internally, they vary in character and thickness, the longest traced for a maximum of 600 metres along strike. The medial and upper occurrences occur within and at the top of the marker, respectively, and the lowest occurrence is in the underlying mafic unit.

The lowest occurrence consists of a stratiform chert bed that consists of jasper and minor carbonate layers in otherwise massive white silica. It is about 5 m thick and can be followed laterally in isolated exposures for about 120 m. The middle siliceous occurrence is about 15 m above the base of the marker interval and exhibits numerous decm-scale vuggy, frothy-looking siliceous beds that alternate with feldspathic sandstone and tuffaceous siltstone (Fig. 6). Parallel, cm-scale felsic ash-rich layers mimic the irregular upper surfaces of some sandstone and siliceous beds, possibly from water-settled airborne ash. Capping the uppermost limestone in the marker

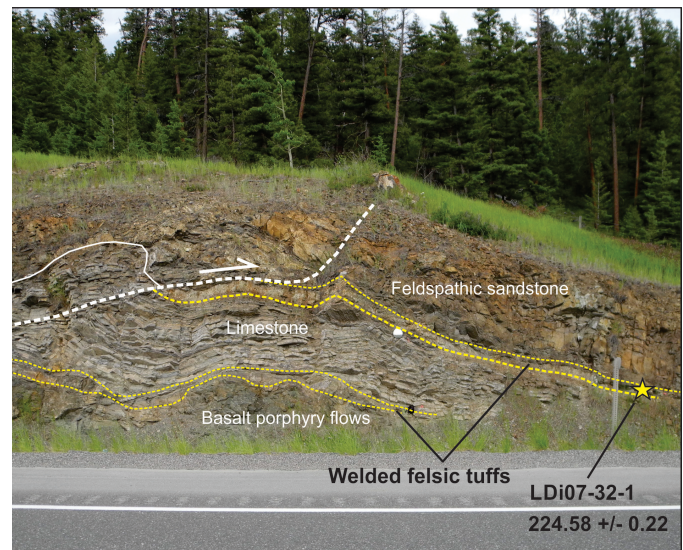


Fig. 5. Rhyolite tuff interlayered with sedimentary and volcanic beds at the base of the marker interval in the upper stratified unit at Castillion Creek, Western belt of the Nicola Group. Sample LDI07-32-1 from welded tuff band with U-Pb TIMS age (see below).

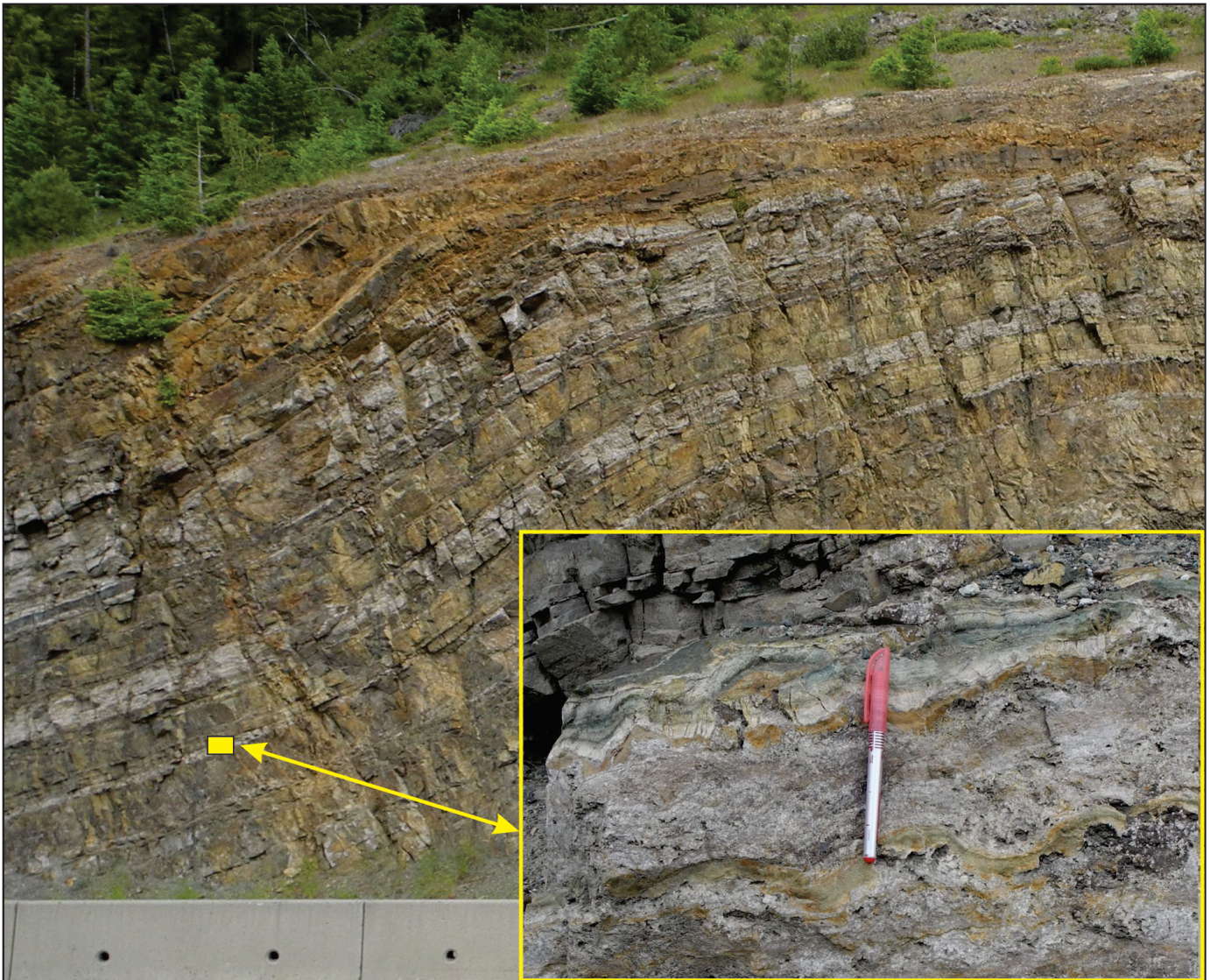


Fig. 6. Grey chert layers interbedded with sandstone and frothy silica (greyish layers) regularly interbedded in the lower part of the marker interval at Castillion Creek, adjacent to the Coquihalla Highway. Height of the exposure is approximately 15 metres. Inset: grey vuggy silica forming frothy-textured layers and interspersed off white ash mantling frothy silica layers with tan siltstone lenses.

unit is a massive 1.5 m thick chert bed, with a basal siliceous mudstone-clast breccia about 25 cm thick. Collectively, these siliceous occurrences are interpreted as repeated exhalations pooled in a relative shallow submarine environment.

Above the marker unit at Castillion Creek is a >1400 m-thick section of mainly volcanic rocks assigned to the upper stratified unit. Dacite and andesite lava flow deposits and related lapilli tuffs are predominant along the east-west ridge leading to Selish Mountain. The flows are commonly finely layered and the tuffs locally display welding. Notably, accretionary lapilli tuff beds are repeated in the section above the marker unit to Selish Mountain and beyond, suggesting much of the section might be subaerial.

2.3. Triassic intrusions

Triassic intrusions that cut the Nicola Group include the Allison pluton (~223 Ma, this study), the Coldwater pluton (~210 Ma, this study) and stocks of the Copper Mountain suite (~205 Ma).

2.3.1. Allison pluton

The Allison pluton underlies the west-central part of the study area where recent mapping shows that it is more extensive than previously recognized (Fig. 2). It is a composite intrusive body, comprising felsic and mafic hornblende-bearing phases. Mafic-rich units range from quartz diorite to hornblende-plagioclase pegmatite. Felsic units range from pink, coarse-grained granite with smoky quartz, to medium-grained, white-weathering tonalite, which tends to cross-cut mafic units. However,

evidence for mingling of mafic and felsic melts is common (see Mihalynuk et al., 2015). In the west-central part of the study area, the Allison pluton cuts and/or thermally alters older rocks consisting mainly of augite porphyry and calcareous sedimentary rocks with felsic tuffaceous intervals and probably provided detrital zircons for younger Nicola Group strata. It is a composite body for which we report the first crystallization age of 223 Ma on a synkinematic granitic phase.

2.3.2. Coldwater pluton

At the south end of the Western belt, intermediate and felsic volcanic rocks thought to be stratigraphically continuous with, but well above the marker unit at Castillion Creek are cut by the Coldwater pluton. The intrusive contact is inferred from local exposures along the south-facing slope of Selish Mountain and from several volcanic rafts on the pluton roof. Bleaching and local chlorite alteration caused by thermal metamorphism appears restricted to be relatively narrow zones, perhaps only 10s of metres wide. The Coldwater pluton is homogeneous, consisting of medium- to coarse-grained equigranular diorite containing plagioclase, and variable amounts of fresh biotite (5-15%) and pyroxene (10-35%). Near the pluton margin the concentration of biotite increases to 20% with a corresponding reduction in grain size. Exposures along the Coquihalla Highway generally weather to a light greyish and appear granodioritic in composition; however, they maintain the same primary mafic mineralogy, roughly in similar proportions as dioritic phases. Rare dikes composed of pink, fine grained granite (20 cm wide) and fine grain diorite (3 m wide) cut the pluton.

2.3.3. Copper Mountain suite

Kilometre-scale dioritic stocks intrude strata along the Central belt and commonly are associated with at least minor porphyry copper-style mineralization. Based on lithology, mineralization and arc-axial location, they are presumed to belong to the ~205 Ma (Logan and Mihalynuk, 2014) Copper Mountain suite (Woodsworth et al., 1992); however, attempts to obtain isotopic crystallization age determinations have so far been unsuccessful.

2.4. Jurassic strata

Youngest Nicola Group strata are apparently overlain by the Shea polymictic conglomerate (≤ 190 Ma, this study), containing abundant intrusive boulders in a maroon, sandy matrix. The Shea conglomerate is lithologically similar to an older conglomerate layer near the base of the Harmon succession that Mihalynuk et al. (2015) also referred to as the 'Shea conglomerate', a practice that is abandoned herein (see Section 3.2.2.4 below). The Harmon conglomerate is restricted to the coarse-grained basal part of maroon epiclastic strata with a detrital zircon maximum age of between ~208 Ma (Mihalynuk et al., 2015) and ~213 Ma (this study).

A conspicuous chert pebble conglomerate (Bates unit; Mihalynuk et al., 2015; <164 Ma, this study), is in apparent thrust contact with various units of the Harmon succession,

and is apparently overthrust by Nicola Group. Lack of a local source for the chert clast-rich conglomerate is puzzling, but the clasts were likely derived from extensive ribbon cherts of the Cache Creek terrane, the closest exposures of which are now 75 km to the northwest. The conglomerate may be tectonostratigraphically analogous to the Tantalus chert clast-bearing conglomerate, which was deposited in mainly alluvial and shallow deltaic settings atop northern Quesnellia and Stikinia, also far from present-day Cache Creek terrane sources (Long, 2015).

2.5. Jurassic intrusions

Throughout most of the northeastern part of the study area, all Eastern belt strata are cut by non-foliated rocks of the Pennask batholith. A 193 Ma U-Pb age from a sample of the intrusion (this study) confirms a previous crystallization age from a locality farther northeast (194 ± 1 Ma, Parrish and Monger, 1992). Pennask batholith is part of a regional suite including the batholithic-scale Bromley pluton and related pegmatite in the southeast part of the study area (193 ± 1 Ma, Parrish and Monger, 1992; 193.6 ± 0.3 Ma, Mihalynuk et al., 2015).

2.6. Cretaceous and Eocene rocks

Unconformably overlying Nicola Group units, volcano-sedimentary strata of the Spences Bridge Group form a continuous belt along the western flank of the Nicola arc (Fig. 2). Revising nomenclature of previous studies, Thorkelson and Rouse (1989) divided the group into a lower unit (Pimainus Formation) consisting of andesitic to rhyolitic volcanic flows and related pyroclastic and epiclastic rocks, and an upper unit (Spius Formation) consisting mainly of amygdaloidal andesitic volcanic flows with minor pyroclastic and epiclastic rocks. The Pimainus Formation is the most common in the study area, where it consists mainly of felsic volcanic rocks and derived epiclastic strata. Volcanic strata in the Spences Bridge Group have consistently yielded isotopic ages of 104 Ma (Thorkelson and Rouse, 1989; Diakow, unpublished data). Dikes presumed to be feeders to the Spences Bridge Group (Mihalynuk et al., 2010, 2015) might point to Pimainus Formation magmatism continuing for a added 1.5 m.y. Thorkelson and Smith (1989) interpreted the Pimainus Formation as a continent margin magmatic arc sequence formed during subduction of a narrow basin, and that the Spius Formation records intraplate shield-type magmatism.

Relicts of a once more extensive veneer of Princeton Group (Eocene) felsic volcanic strata are found sporadically throughout the area, but intrusive centres related to this magmatism are uncommon. One such stock is related to mineralization at the Snowstorm prospect (ca. 1917) which, produced minor base metals from sulphides in a quartz vein stockwork (Groves, 1989). Snowstorm adits are drifted into an extensively clay-altered porphyritic intrusion that crystallized at ~53 Ma (this study). This age is consistent with previous Eocene cooling ages (Armstrong and Petö, 1981) and the intrusion is probably comagmatic with Princeton Group volcanic strata (Ickert et al.,

2009; Mihalynuk et al., 2014a, b).

3. Geochronology

Below we present seven new U-Pb zircon ages from the Eastern and Central belts, one $^{40}\text{Ar}/^{39}\text{Ar}$ age from the Western belt, and five unpublished U-Pb zircon ages from a previous study of the Western belt (Diakow and Barrios, 2008). We also present ages from three post-Nicola Group units (the Pennask batholith, Osprey volcanic unit, and the Snowstorm porphyry). These data compliment previous results reported in Mihalynuk and Logan (2013 a,b) and Mihalynuk et al. (2014a, b). The analyses were completed at the Pacific Centre for Geochemical and Isotopic Research (University of British Columbia, Vancouver).

3.1. Methods

Complete procedures are reported in a companion publication (Friedman et al., 2016) and only abridged methods are presented here.

3.1.1. U-Pb zircon chemical abrasion thermal ionization mass spectrometry (CA-TIMS)

CA-TIMS procedures are modified from Mundil et al. (2004), Mattinson (2005) and Scoates and Friedman (2008). Rock samples underwent standard mineral separation procedures, and zircon separates were handpicked in alcohol. The clearest, crack- and inclusion-free grains were selected, photographed, and then annealed at 900°C for 60 hours. Annealed grains were chemically abraded, spiked with a $^{233-235}\text{U}$ - ^{205}Pb tracer solution (EARTHTIME ET535), and then dissolved. Resulting solutions were dried and loaded onto Re filaments (Gerstenberger and Haase, 1997).

Isotopic ratios were measured by a modified single collector VG-54R or 354S thermal ionization mass spectrometer equipped with analogue Daly photomultipliers. Analytical blanks were 0.2 pg for U and up to 1.0 pg for Pb. U fractionation was determined directly on individual runs using the ET535 mixed $^{233-235}\text{U}$ - ^{205}Pb isotopic tracer. Pb isotopic ratios were corrected for fractionation of 0.30%/amu, based on replicate analyses of NBS-982 reference material and the values recommended by Thirlwall (2000). Data reduction used the Excel™-based program of Schmitz and Schoene (2007). Standard concordia diagrams were constructed and regression intercepts and weighted averages calculated with Isoplot (Ludwig, 2003). All errors are quoted at the 2σ or 95% confidence level, unless otherwise noted. Isotopic ages were calculated with the decay constants $\lambda^{238}=1.55125\text{E}-10$ and $\lambda^{235}=9.8485\text{E}-10$ (Jaffe et al, 1971). EARTHTIME U-Pb synthetic solutions were analysed on an ongoing basis to monitor accuracy.

3.1.2. U-Pb zircon LA – ICPMS

Sample material selected was preferentially medium to coarse-grained sandstones which are expected to have the best likelihood of containing detrital zircons. Following collection, samples were isolated, double wrapped in plastic bags and

placed in buckets. Samples were cleaned by washing followed by air abrading. Zircons were analyzed using laser ablation (LA) ICPMS methods using the techniques described by Tafti et al. (2009). Instrumentation comprised a New Wave UP-213 laser ablation system and a ThermoFinnigan Element2 single collector, double-focusing, magnetic sector ICP-MS. All zircons greater than about 50 microns in diameter were picked from the mineral separates and mounted in an epoxy puck along with several grains of the Plešovice (337.13 ± 0.13 Ma, Sláma et al., 2007), and Temora2 (416.78 ± 0.33 Ma) zircon standards and brought to a very high polish. Before analysis, the surface of the mount was washed for 10 minutes with dilute nitric acid and rinsed in ultraclean water. The highest quality portions of each grain selected for analysis were free of alteration, inclusions, or possible inherited cores. Line scans rather than spot analyses were employed in order to minimize elemental fractionation during the analyses. A laser power level of 40% and a 25 mm spot size was used. Backgrounds were measured with the laser shutter closed for ten seconds, followed by data collection with the laser firing for approximately 35 seconds. The time-integrated signals were analysed using Lolite software (Patton et al, 2011), which automatically subtracts background measurements, propagates all analytical errors, and calculates isotopic ratios and ages. Corrections for mass and elemental fractionation are made by bracketing analyses of unknown grains with replicate analyses of the Plešovice zircon standard. A typical analytical session consisted of four analyses of the Plešovice standard zircon, followed by two analyses of the Temora2 zircon standard, five analyses of unknown zircons, two standard analyses, then five unknown analyses. Each session was completed with two Temora2 zircon standards and four Plešovice standard analyses. The Temora2 zircon standard was analysed as an unknown to monitor the reproducibility of the age determinations on a run-to-run basis (see Friedman et al., 2016).

For plotting and interpretation of detrital zircon analytical results the ISOPLOT software of Ludwig (2003) is commonly used. Acceptance of the youngest probability density peak generated by Isoplot 4.15 as the minimum depositional age is typically a conservative approach, but not always (e.g., young single grain outlier in GMC14-60-2 identified by Isoplot as a sub-population). A more common issue may be the inclusion of multiple populations within a single peak. Bandwidth is an important consideration in resolving population peaks, and proper bandwidth selection is important in identification of sub-populations. Routines such as Unmix in Isoplot 4.15 can be applied to help identify sub-populations, but this routine was not used herein. To evaluate probability density distribution plots, we examined each sample dataset and considered criteria like smallest error envelopes and % discordance of individual zircon analyses in an attempt to reveal the youngest real zircon population(s). We applied a filter to some samples such that the youngest sub-population grains selected have 2σ errors less than 5% of the zircon age determination, and with $^{207}\text{Pb}/^{235}\text{U}$ and $^{206}\text{Pb}/^{238}\text{U}$ age determinations that differ by less than 1σ. We

also considered zircon spot chemistry, placing more confidence in young sub-populations with homogeneous Pb, Th and U isotope contents as a percentage of the analytical counts per second compared to the range of values for that sample.

3.1.3. $^{40}\text{Ar}/^{39}\text{Ar}$

Mineral separates were hand picked, washed in nitric acid, rinsed in de-ionized water, dried, wrapped in aluminum foil and stacked in an irradiation capsule with similar-aged samples and neutron flux monitors (Fish Canyon tuff sanidine, 28.02 Ma; Renne et al., 1998). The samples were irradiated at the McMaster Nuclear Reactor in Hamilton, Ontario, for 90 MWh, with a neutron flux of approximately 3 by 10^{16} neutrons/cm²/s.

The sample was analyzed at the Noble Gas Laboratory, Pacific Centre for Isotopic and Geochemical Research, The University of British Columbia, Vancouver. The mineral separate was step heated at incrementally higher powers in the defocused beam of a 10 W CO₂ laser (New Wave Research MIR10) until fused. The gas evolved from each step was analyzed by a VG5400 mass spectrometer equipped with an ion-counting electron multiplier. All measurements were corrected for total system blank, mass spectrometer sensitivity, mass discrimination, radioactive decay during and subsequent to irradiation, as well as interfering Ar from atmospheric contamination and the irradiation of Ca, Cl and K (isotope production ratios: $[\text{}^{40}\text{Ar}/^{39}\text{Ar}]_{\text{K}}=0.0302 \pm 0.00006$; $[\text{}^{37}\text{Ar}/^{39}\text{Ar}]_{\text{Ca}}=1416.4 \pm 0.5$; $[\text{}^{36}\text{Ar}/^{39}\text{Ar}]_{\text{Ca}}=0.3952 \pm 0.0004$, Ca/K=1.83 \pm 0.01 $[\text{}^{37}\text{Ar}_{\text{Ca}}/^{39}\text{Ar}_{\text{K}}]$).

The plateau and correlation ages were calculated using Isoplot v. 3.00 (Ludwig, 2003). Errors are quoted at the 2 σ (95% confidence) level and are propagated from all sources except mass spectrometer sensitivity and age of the flux monitor. The best statistically justified plateau and plateau age were picked based on the following criteria.

- three or more contiguous steps comprising more than 30% of the ^{39}Ar
- the probability of fit of the weighted mean age greater than 5%
- the slope of the error-weighted line through the plateau ages equals zero at 5% confidence
- the ages of the two outermost steps on a plateau are not significantly different from the weighted-mean plateau age (at 1.8 σ , six or more steps only)
- the outermost two steps on either side of a plateau must not have nonzero slopes with the same sign (at 1.8 σ , nine or more steps only).

3.2. Results

An overview of geochronologic results is presented in Table 1 and a synthesis of all Triassic age data is presented in Figure 7. Complete raw data tables along with UTM coordinates, procedural blanks and standards, cathode luminescence imagery for many of the zircons analyzed, and supporting diagrams such as detrital zircon isochron plots, and Ar release spectra can be found in Friedman et al. (2016).

3.2.1. Zircon CA-TIMS crystallization and $^{40}\text{Ar}/^{39}\text{Ar}$ cooling ages

Sampling for high resolution TIMS geochronology focused on intrusive rocks or felsic extrusive rocks of primary volcanic origin or very immature, reworked volcanic strata in which quartz phenocrysts are present and felsic clasts predominate.

3.2.1.1. Sample MMI14-55-13 (U1), Western belt rhyolite tuffite near Coalmont; 238.6 \pm 0.3 Ma

Between Princeton and Tulameen (Fig. 2), rhyolite flows and tuffs form a belt >10 km long and <2 km wide. Rhyolite flows are rarely quartz-phyric, but typically pyritic and altered with secondary white mica and clays in white, rust and yellow weathered exposures. Immediately east of Coalmont (adjacent the old town dump) the felsic unit appears to be slightly reworked into pebbly sandstone (tuffite) and interlayered with locally pillowed basalt flow and breccia. In one outcrop, the felsic unit has laminae of Fe>Cu sulphides, interpreted as exhalite (Mihalynuk et al., 2014a). Geochronological analysis of the felsic volcanoclastic unit would provide an age of the felsic belt and possible volcanogenic sulphide mineralization. In addition, an age would test a suspected correlation with very similar rhyolitic rocks at Missezula Mountain (Mihalynuk et al., 2015) and farther north, near the Ketchikan porphyry prospect (see below; Sample MMI14-23-15) about 30 km to the northeast, across the Nicola arc.

Sample MMI14-55-13 was collected from the base of a cliff on the eastern outskirts of Coalmont. Although zircons were sparse and fine grained (<50 microns in diameter), they provided a precise U-Pb age of 238.6 \pm 0.3 Ma (Fig. 8, Table 2). This age is nearly identical (within the limits of error) to the 238.1 \pm 0.3 Ma age of pyritic felsic lapilli tuff on the east flank of Missezula Mountain (see Sample MMI13-30-4; Mihalynuk et al., 2015) providing compelling support for the lithological correlation. Together, these determinations provide the oldest crystallization ages known from the Nicola Group.

3.2.1.2. Sample LDi12-1-9 (U2), Western belt, dacite tuff at top of marker unit at Hamilton Creek; 224.51 \pm 0.15 Ma

Sample LDi12-1-9 is from a dacitic lapilli tuff marking the highest exposure in the Hamilton Creek section. This dacite contains light colored felsic-lithic fragments and scarce quartz grains. Five overlapping analyses give a weighted $^{206}\text{Pb}/^{238}\text{U}$ age of 224.51 \pm 0.15 Ma (Fig. 9, Table 3). Limestone sampled stratigraphically below the dated tuff, contain a diverse fauna, including the bivalve *Halobia* sp., and conodont species with an age range of latest Carnian to early Norian (see collection F4, Table 1 in Preto, 1979).

3.2.1.3. Sample LDi07-7-5 (U3), Western belt, dacite near base of marker unit at Iron Mountain; 223.55 \pm 0.29 Ma

Sample LDi07-7-5 was collected from a accretionary lapilli tuff bed 8 m above the base of the marker interval at Iron Mountain (Fig. 4). The weighted $^{206}\text{Pb}/^{238}\text{U}$ age, determined

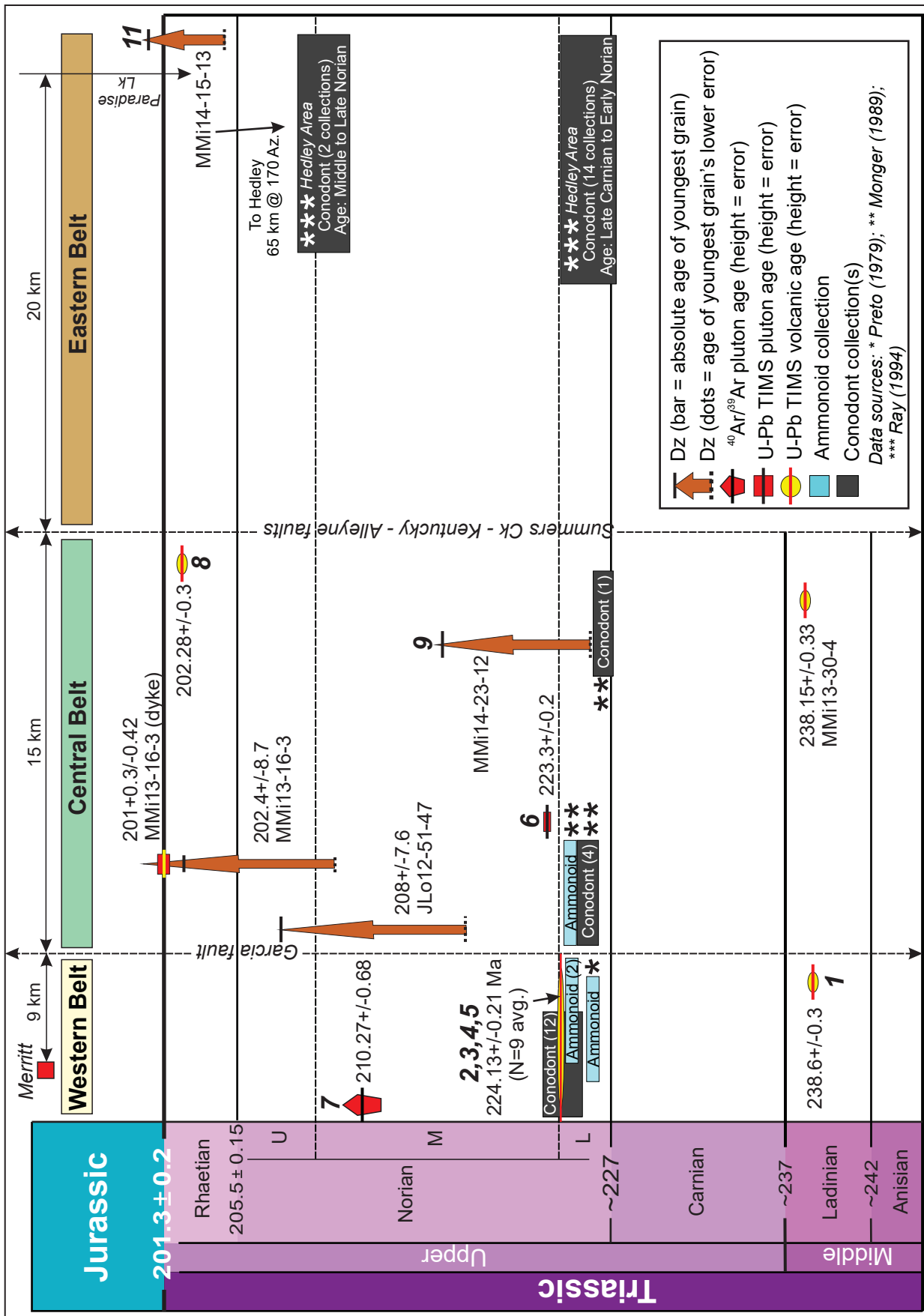


Fig. 7. Time-space distribution of radiometric and biogeochronologic ages for the southern Nicola arc, including unpublished fossil determinations and those reported in Ray and Dawson (1994), and new data presented in this report. Nicola arc belts are those of Preto (1979). Crystallization ages are shown with 2σ errors (solid bars). Detrital zircon ages are from the youngest grains, with the lower extent of arrows portraying 2σ error and the maximum age of deposition. Time scale after Cohen et al. (2013) showing an updated time pick for the Rhaetian lower boundary (Wotzlaw et al., 2014). Isotopic ages are identified by sample numbers cross referenced to Table 1.

Table 1. Synopsis of new ages presented herein; for details see Friedman et al. (2016).

Map No.	Sample No.	Type	Unit / Problem Addressed	age
Magmatic crystallization ages, Nicola Group				
U1	MMI15-53-13	U-Pb	Western belt; rhyolite tuffite near exhalite at Coalmont	238.6 ± 0.3 Ma
U2	LDi12-1-9	U-Pb	Western belt; dacite tuff at top of Hamilton Creek marker	224.51 ± 0.15 Ma
U3	LDi07-7-5	U-Pb	Western belt; dacite near base of Iron Mountain marker	223.55 ± 0.29 Ma
U4	LDi07-7-2	U-Pb	Western belt; rhyolite at the top of Iron Mountain marker	224.11 ± 0.26 Ma
U5	LDi07-32-1	U-Pb	Western belt; welded rhyolite tuff at base of Castillion Creek marker	224.58 ± 0.22 Ma
U6	MMI14-50-2	U-Pb	Central belt; Allison pluton; synkinematic pegmatitic dike cuts border phase only K-Ar determinations previously	223.3 ± 0.2 Ma
A7	LDi07-20-3	Ar/Ar	Western belt; Coldwater pluton cuts and thereby constrains age of upper stratified unit; biotite cooling age	210.27 ± 0.68 Ma
U8	MMI14-62-4	U-Pb	Central belt; Zig dacite lapilli tuff	202.28 ± 0.26 Ma
Sedimentary units, detrital zircon maximum depositional ages; Nicola Group				
D9	MMI14-23-15	U-Pb	Central belt; sharpstone conglomerate derived from Nicola felsic source Confirm source is felsic arc component which so far are ~239 Ma	<227 Ma
D10	LDi14-60-3	U-Pb	Central belt; Harmon succession; sandstone immediately below Voght basalt marker – determine age range of Voght clastic strata	<213 Ma
D11	MMI14-15-13	U-Pb	Eastern belt; fine siliciclastic unit presumed mid to upper Triassic	<202 Ma
Magmatic crystallization ages; intrusions cutting Nicola Group				
U12	MMI14-19-3	U-Pb	Pennask batholith gabbroic pegmatite with minor copper mineralization	193.1 ± 0.2 Ma
U13	MMI14-59-12	U-Pb	Osprey volcanic unit	163.2 ± 0.2 Ma
U14	MMI14-53-2	U-Pb	Snowstorm altered “Otter intrusive suite”, cut by base metal sulphide-quartz stockwork, with open space textures	53.36 ± 0.07 Ma
Sedimentary units, detrital zircon maximum depositional ages; younger than Nicola Group				
D15	MMI14-62-1	U-Pb	Shea conglomerate, extensive erosional deposit above Nicola	<190, possibly ~185 Ma
D16	GMC14-60-2	U-Pb	Bates conglomerate, predominantly chert pebbles lacking a local source	<163, possibly ~134 Ma

*Sample details UTM Easting and UTM Northing as well as complete data tables can be found in Friedman et al. (2016).

from four overlapping zircon fractions on concordia is 223.55 ± 0.29 Ma (Fig. 10, Table 4).

3.2.1.4. Sample LDi07-7-2 (U4), Western belt, rhyolite at top of marker unit at Iron Mountain; 224.11 ± 0.26 Ma

Sample LDi07-7-2 is from a lenticular rhyolite unit (80 m wide by 220 m long) believed to depositionally overlie the mainly sedimentary upper part of the marker unit at Iron Mountain (Figs. 3 and 4). A 25 m wide vegetated area separates underlying feldspathic sandstones from aphanitic light grey-green rhyolite. The rhyolite gives a weighted $^{206}\text{Pb}/^{238}\text{U}$ age of 224.11 ± 0.26 Ma interpreted from two overlapping analyses of a younger group (Fig. 11, Table 5). This age is older than the age determined from the dacite near the base of the marker interval at Iron Mountain (see above) which, together with the slightly older population (Fig. 11), may indicate that the zircons are xenocrysts or antecrysts from an older partly crystallized melt from which the rhyolite later erupted.

3.2.1.5. Sample LDi07-32-1 (U5), Western belt, welded rhyolite tuff near base of marker unit at Castillion Creek; 224.58 ± 0.22 Ma

At the base of the marker interval at Castillion Creek, are two rhyolite welded tuff beds that are separated by a limestone

layer; Sample LDi07-32-1 is from the upper of the two tuffs (Fig. 5). The weighted $^{206}\text{Pb}/^{238}\text{U}$ age on four overlapping U-Pb TIMS zircon analyses is 224.58 ± 0.22 Ma (Fig. 12, Table 6).

3.2.1.6. Sample MMI14-50-2 (U6), Central belt, Allison pluton; 223.3 ± 0.2 Ma

Sample MMI14-50-2 was collected from the interior of a northeast-oriented dioritic zone (2.5 km wide) near the contact with a screen of mafic country rock (minimum dimension of ~100 m wide), possibly a part of the pluton floor. A weak to moderate fabric in the country rock is strongly overprinted by granoblastic mafic minerals (predominantly hornblende ± pyroxene, magnetite, garnet and sparse clots of very coarse biotite), and these grade into zones of varitextured diorite. Leucogranitic dikes cut the diorite. Planar dikes (decimeters wide) coalesce in the area sampled, and display medium-grained to pegmatitic textures with oriented tabular quartz-feldspar crystal growth on their margins and ribboned quartz in their interiors (Figs. 13 a, b, c). Quartz ribbons have sutured grain boundaries with strained subgrains along them. These textures are evidence of solid state ductile deformation (Duke et al., 1988; Paterson et al., 1989) and a change from magmatic fabrics to tectonic fabric development.

Although the regional importance of this synkinematic fabric

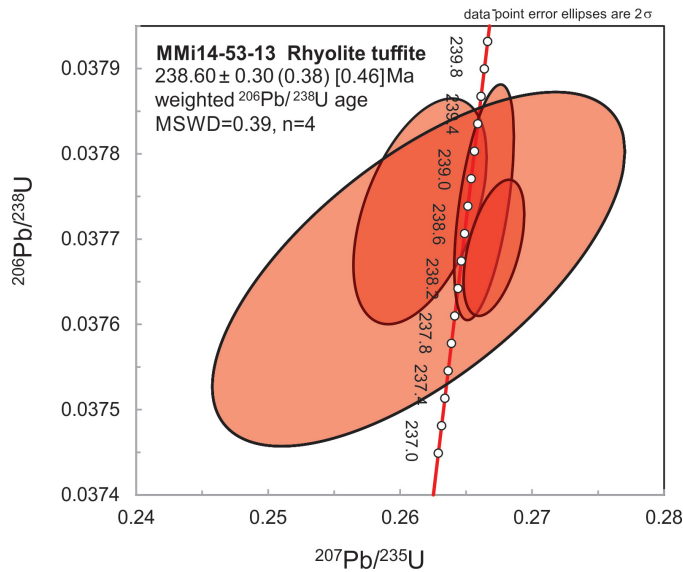


Fig. 8. U-Pb concordia diagram showing TIMS zircon U-Pb age results from sample MMI14-53-13, rhyolite lapilli tuff at Coalmont, Western belt.

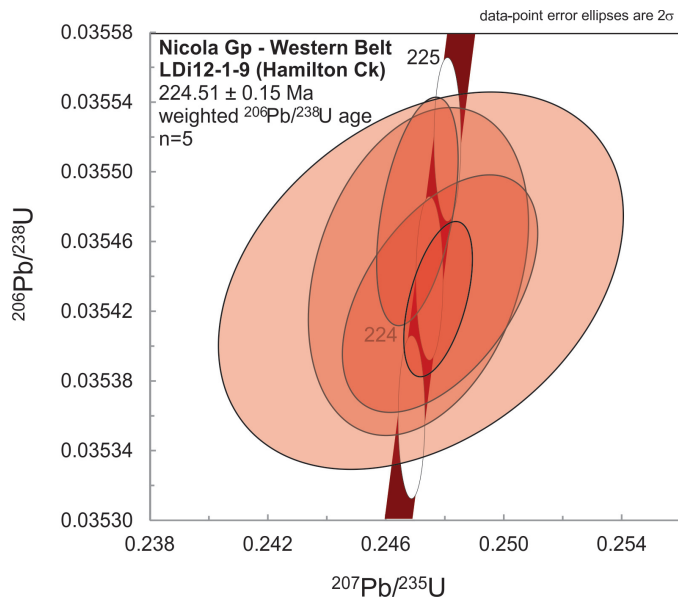


Fig. 9. Concordia plot for U-Pb TIMS data from single zircons, sample LDi12-1-9 (dacite tuff at top of Hamilton Creek marker, Western belt). Weighted age 224.51 ± 0.15 Ma based on $^{206}\text{Pb}/^{238}\text{U}$ ages of 5 grains. Concordia bands include 2σ errors of U decay constants.

has yet to be established, dating a cross-cutting leucocratic phase of the Allison pluton provided an opportunity to corroborate existing hornblende and muscovite K-Ar cooling ages of 204 ± 10 to 207 ± 10 Ma (Preto, 1979; recalculated by Breitsprecher and Mortensen, 2004), while dating the deformational fabric. Chlorite alteration is ubiquitous at the sample site and elsewhere in the pluton, together with lesser epidote, rendering analysis of K-bearing phases unreliable.

A crystallization age has been determined from three zircons overlapping concordia at 223.3 ± 0.2 Ma (Fig. 14, Table 7). It

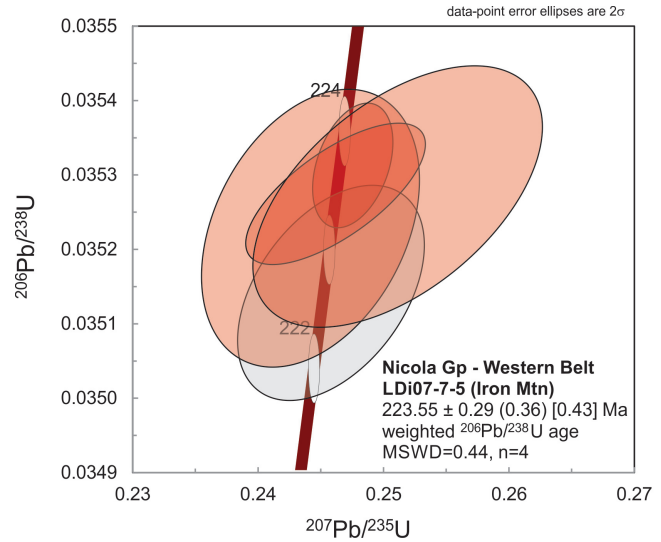


Fig. 10. Concordia plot for U-Pb TIMS data from single zircons, sample LDi07-7-5 (dacite at base of the marker interval at Iron Mountain, Western belt; see Fig. 4). Weighted age 223.55 ± 0.29 Ma based on $^{206}\text{Pb}/^{238}\text{U}$ ages of 4 grains. Concordia bands include 2σ errors of U decay constants.

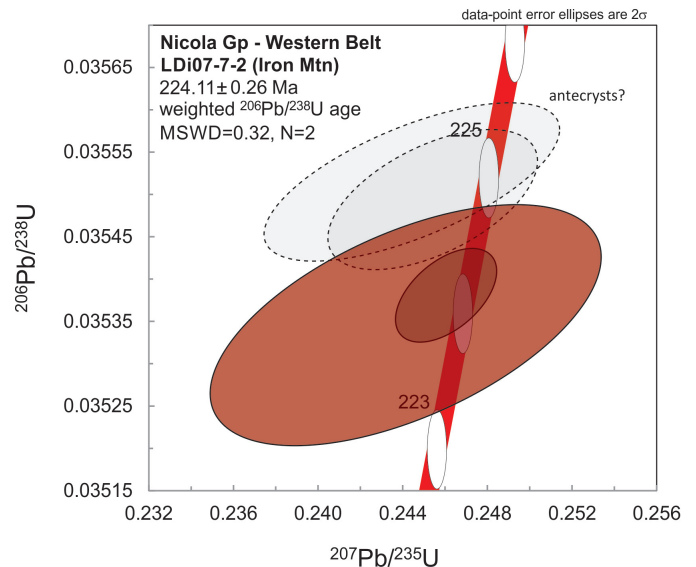


Fig. 11. Concordia plot for U-Pb TIMS data from single zircons, sample LDi07-7-2 (rhyolite at the top of the marker interval at Iron Mountain, Western belt; see Fig. 4). Weighted age 224.11 ± 0.26 Ma based on $^{206}\text{Pb}/^{238}\text{U}$ ages of 2 grains from the younger population. Concordia bands include 2σ errors of U decay constants.

is older than the oldest limit of error for previously reported K-Ar cooling ages, but consistent with a population of detrital zircons from basal conglomerate of the Spences Bridge Group unconformably overlying the pluton's eastern margin (see Mihalynuk et al., 2014). This age is very similar similar to ages (e.g., 222.71 ± 0.22 Ma) from Burgess Creek tonalite to diorite stock at the northeast margin of the Granite Mountain batholith (adjacent the Gibraltar Cu-Mo porphyry deposit, Fig. 1), which

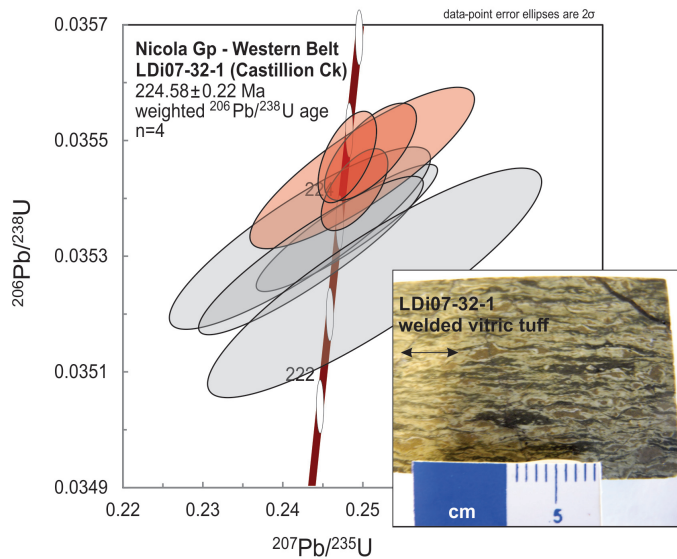


Fig. 12. Concordia plot for U-Pb TIMS data from single zircons, sample LDi07-32-1 (welded rhyolite tuff at base of the marker interval at Castillion Creek, Western belt). Weighted age 224.58 ± 0.22 Ma based on $^{206}\text{Pb}/^{238}\text{U}$ ages of 4 grains. Concordia bands include 2σ errors of U decay constants. Inset: Collapsed vitriclasts define eutaxitic texture in welded tuff.

also displays synplutonic deformation fabrics cut by younger undeformed intrusive phases (Schiarizza, 2014, 2015, pers. comm. 2016).

3.2.1.7. Sample LDi07-20-3 (A7), Western belt, Coldwater pluton; 210.27 ± 0.68 Ma

Sample LDi07-20-3, from near the centre of the Coldwater pluton, is a medium-grained equigranular quartz diorite containing 20% vitreous biotite. A biotite separate yields a plateau, formed by 80.7% of ^{39}Ar gas in 10 steps from which an age of 210.27 ± 0.68 Ma is calculated (Fig. 15, Table 8). Because the pluton lacks evidence of secondary alteration, or structural disruption leading to thermal resetting, we infer that the cooling age approximates a crystallization age for the pluton.

The Coldwater pluton cuts the upper stratified unit of the Western belt at Selish Mountain, bracketing deposition to between ~ 224 Ma (age from the base of the marker interval at Castillion Creek) and ~ 210 Ma.

3.2.1.8. Sample MMI14-62-4 (U8), Central belt, Zig volcanic unit, dacite 202.3 ± 0.3 Ma

In the northern part of the Central belt are pyroclastic deposits of high-silica andesite to dacite composition, readily distinguished by phenocrysts including biotite, quartz and apatite. It is referred to as the Zig unit (Mihalynuk et al., 2015), after the Zig mineral prospect (specifically NOR30), where several old pits excavated calcite-quartz-chalcocite veins up to 20 cm thick. Re-Os isotopic analysis of semi-massive chalcocite in these veins has returned an age of 215 ± 2 Ma

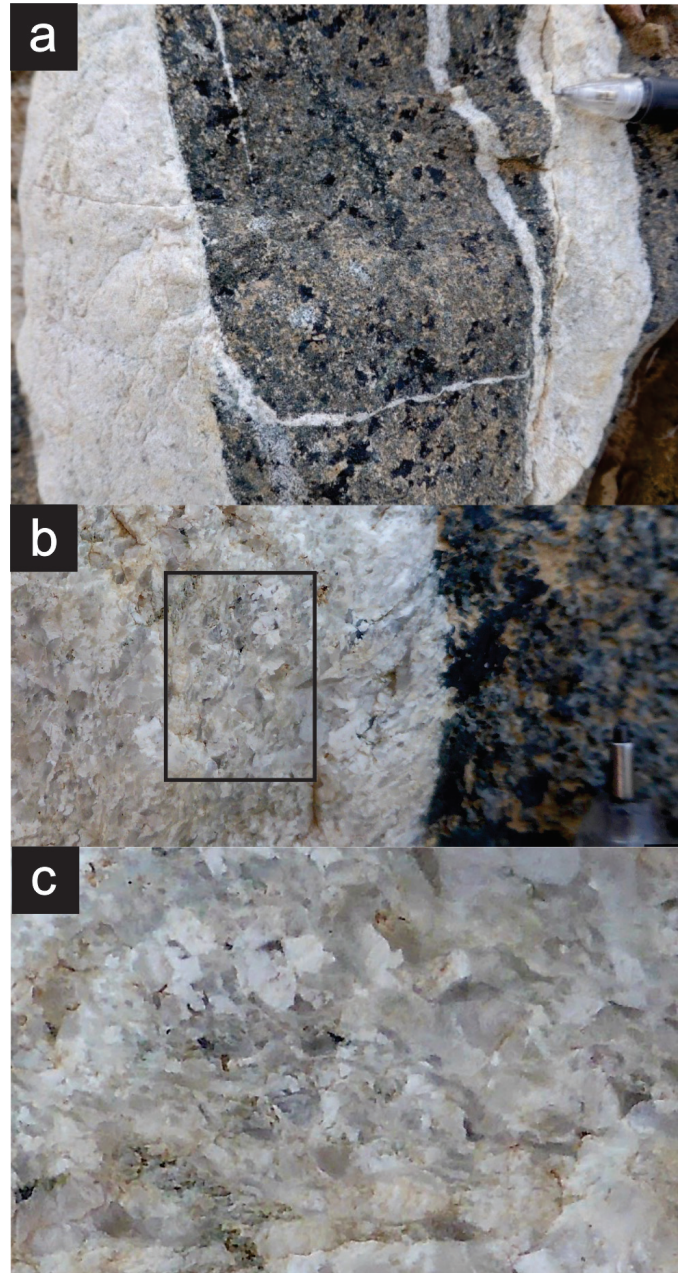


Fig. 13. Allison pluton; leucogranite dikes at sample site MMI14-50-2. **a)** Coalcescing dikelets. **b)** Dike close-up showing comb texture mineral growth at the margin (0.5 mm mechanical pencil point for scale). **c)** subsolidus ribbon quartz near the dike centre.

(R.A. Creaser, unpublished data).

Sample MMI14-62-4 was collected about 5 km to the south along strike of the NOR30 prospect (Fig. 2), in a bluff section of medium-grained plagioclase-bearing tuff containing $\sim 1\%$ red apatite grains (≤ 3 mm in diameter), commonly euhedral with grey rims, and $\sim 0.5\%$ euhedral biotite booklets (≤ 4 mm in diameter). Where sampled, the unit displays characteristic weak and patchy chlorite and epidote alteration, but unlike the unit near NOR30, quartz phenocrysts are conspicuously lacking. Lithic fragments are rounded, perhaps indicating reworking,

Table 2. U-Th-Pb analytical results for MM114-53-13.

Sample	Compositional Parameters				Radiogenic Isotope Ratios						Isotopic Ages											
	U ppm	Pb ppm	Th/U	Pb/U	$\frac{^{206}\text{Pb}}{^{206}\text{Pb}}$	$\frac{^{207}\text{Pb}}{^{206}\text{Pb}}$	$\frac{^{208}\text{Pb}}{^{206}\text{Pb}}$	$\frac{^{207}\text{Pb}}{^{235}\text{U}}$	$\frac{^{206}\text{Pb}}{^{238}\text{U}}$	corr. coef.	$\frac{^{207}\text{Pb}}{^{206}\text{Pb}}$	\pm	$\frac{^{207}\text{Pb}}{^{235}\text{U}}$	\pm	$\frac{^{206}\text{Pb}}{^{238}\text{U}}$	\pm						
(a)	(i)	(j)	(b)	(c)	(c)	(c)	(c)	(e)	(f)	(e)	(f)	(e)	(f)	(g)	(f)	(g)	(f)					
MM114-53-13																						
A	0.0013	114	4.9	0.298	0.2334	95.91%	7	0.82	452	0.093	0.0503	1.463	0.03773	0.287	0.478	207.3	33.9	235.9	3.3	238.76	0.67	
B	0.0016	106	4.1	0.255	0.2664	98.65%	21	0.30	1369	0.081	0.0512	0.582	0.2664	0.299	0.556	249.1	13.4	239.8	1.5	238.83	0.70	
C	0.0018	92	3.7	0.337	0.2612	98.17%	16	0.40	1014	0.108	0.0514	0.637	0.2671	0.173	0.495	258.8	14.6	240.4	1.5	238.50	0.41	
E	0.0009	47	2.3	0.112	0.0661	90.08%	2	0.60	186	0.035	0.0503	4.598	0.2614	4.885	0.03766	4.451	210.5	106.6	235.8	10.3	238.34	1.05

(a) A, B etc. are labels for fractions composed of single zircon grains or fragments; all fractions annealed and chemically abraded after Mattinson (2005) and Scoates and Friedman (2008).
 (b) Model Th/U ratio calculated from radiogenic $^{206}\text{Pb}/^{206}\text{Pb}$ ratio and $^{207}\text{Pb}/^{235}\text{U}$ age.
 (c) Pb* and Pbc represent radiogenic and common Pb, respectively; mol % $^{206}\text{Pb}^*$ with respect to radiogenic, blank and initial common Pb.
 (d) Measured ratio corrected for spike and fractionation only. Mass discrimination of $0.30\% \pm 0.05\%$ amu based on analysis of NBS-982; all Daily analyses.
 (e) Corrected for fractionation, spike, and common Pb; up to 1 pg common Pb was assumed to be procedural blank: $^{206}\text{Pb}/^{206}\text{Pb} = 18.50 \pm 1.0\%$; $^{207}\text{Pb}/^{206}\text{Pb} = 15.50 \pm 1.0\%$; $^{208}\text{Pb}/^{206}\text{Pb} = 38.40 \pm 1.0\%$ (1 σ errors).
 (f) Errors are 2-sigma, propagated using the algorithms of Schmitz and Schoene (2007) and Crowley et al. (2007).
 (g) Calculations are based on the decay constants of Jaffey et al. (1971). $^{206}\text{Pb}/^{238}\text{U}$ and $^{207}\text{Pb}/^{206}\text{Pb}$ ages corrected for initial disequilibrium in $^{230}\text{Th}/^{238}\text{U}$ using Th/U [magma] = 3.
 (h) Corrected for fractionation, spike, and blank Pb only.
 (i) Nominal fraction weights estimated from photomicrographic grain dimensions, adjusted for partial dissolution during chemical abrasion.
 (j) Nominal U and total Pb concentrations subject to uncertainty in photomicrographic estimation of weight and partial dissolution during chemical abrasion.

Table 3. U-Th-Pb analytical results for LD112-1-9.

Sample	Compositional Parameters				Radiogenic Isotope Ratios						Isotopic Ages										
	U mg	Pb mg	Th/U	Pb/U	$\frac{^{206}\text{Pb}}{^{206}\text{Pb}}$	$\frac{^{207}\text{Pb}}{^{206}\text{Pb}}$	$\frac{^{208}\text{Pb}}{^{206}\text{Pb}}$	$\frac{^{207}\text{Pb}}{^{235}\text{U}}$	$\frac{^{206}\text{Pb}}{^{238}\text{U}}$	corr. coef.	$\frac{^{207}\text{Pb}}{^{206}\text{Pb}}$	\pm	$\frac{^{207}\text{Pb}}{^{235}\text{U}}$	\pm	$\frac{^{206}\text{Pb}}{^{238}\text{U}}$	\pm					
(a)	(i)	(j)	(b)	(c)	(c)	(c)	(c)	(e)	(f)	(e)	(f)	(e)	(f)	(g)	(f)	(g)	(f)				
LD112-1-9																					
A	0.0052	74	2.7	0.257	0.5723	98.42%	18	0.75	1172	0.081	0.050557	1.200	0.247068	0.219	0.293	220.70	27.75	224.19	2.51	224.52	0.48
B	0.0036	54	2.0	0.228	0.2890	97.93%	13	0.50	893	0.072	0.050728	1.031	0.247809	0.158	0.509	228.47	23.82	224.79	2.22	224.44	0.35
C	0.0048	137	4.9	0.353	0.9720	99.65%	83	0.28	5298	0.112	0.050501	0.413	0.247036	0.152	0.459	218.14	9.56	224.17	0.93	224.74	0.33
D	0.0023	50	1.8	0.214	0.1690	97.89%	13	0.30	876	0.068	0.050582	2.216	0.247151	0.251	0.344	221.83	51.25	224.26	4.61	224.49	0.55
E	0.0063	146	8.3	0.2495	1.3558	99.21%	59	0.88	2352	0.793	0.050718	0.345	0.247739	0.104	0.517	228.02	7.98	224.74	0.78	224.42	0.23

(a) A, B etc. are labels for fractions composed of single zircon grains or fragments; all fractions annealed and chemically abraded after Mattinson (2005) and Scoates and Friedman (2008).
 (b) Model Th/U ratio calculated from radiogenic $^{206}\text{Pb}/^{206}\text{Pb}$ ratio and $^{207}\text{Pb}/^{235}\text{U}$ age.
 (c) Pb* and Pbc represent radiogenic and common Pb, respectively; mol % $^{206}\text{Pb}^*$ with respect to radiogenic, blank and initial common Pb.
 (d) Measured ratio corrected for spike and fractionation only. Mass discrimination of 0.25% amu based on analysis of NBS-982; all Daily analyses.
 (e) Corrected for fractionation, spike, and common Pb; all common Pb (up to -0.9 pg) was assumed to be procedural blank: $^{206}\text{Pb}/^{206}\text{Pb} = 18.50 \pm 1.0\%$; $^{207}\text{Pb}/^{206}\text{Pb} = 15.50 \pm 1.0\%$; $^{208}\text{Pb}/^{206}\text{Pb} = 38.40 \pm 1.0\%$ (all uncertainties 1-sigma).
 (f) Errors are 2-sigma, propagated using the algorithms of Schmitz and Schoene (2007) and Crowley et al. (2007).
 (g) Calculations are based on the decay constants of Jaffey et al. (1971). $^{206}\text{Pb}/^{238}\text{U}$ and $^{207}\text{Pb}/^{206}\text{Pb}$ ages corrected for initial disequilibrium in $^{230}\text{Th}/^{238}\text{U}$ using Th/U [magma] = 3.
 (h) Corrected for fractionation, spike, and blank Pb only.
 (i) Nominal fraction weights estimated from photomicrographic grain dimensions, adjusted for partial dissolution during chemical abrasion.
 (j) Nominal U and total Pb concentrations subject to uncertainty in photomicrographic estimation of weight and partial dissolution during chemical abrasion.

Table 4. U-Th-Pb analytical results for LDi07-7-5.

Sample	Compositional Parameters										Radiogenic Isotope Ratios						Isotopic Ages							
	Wt.	U	Pb	Th	²⁰⁶ Pb*	mol %	Pb*	Pb _c	Pb _c	Pb _c	Pb _c	²⁰⁸ Pb	²⁰⁷ Pb	²⁰⁶ Pb	corr.	²⁰⁷ Pb	²⁰⁶ Pb	²³⁵ U	²³⁸ U	²⁰⁶ Pb				
	mg	ppm	ppm	U	x10 ⁻¹³ mol	²⁰⁶ Pb*	Pb _c	(pg)	(pg)	(pg)	(pg)	²⁰⁶ Pb	²⁰⁷ Pb	²⁰⁶ Pb	% err	²⁰⁶ Pb	²³⁸ U	% err	²⁰⁶ Pb	²³⁵ U	% err	²⁰⁶ Pb		
(a)	(i)	(j)	(j)	(b)	(c)	(c)	(c)	(c)	(c)	(d)	(e)	(e)	(f)	(f)	(f)	(g)	(g)	(f)	(g)	(f)	(g)	(f)	(g)	(f)
LDi07-7-5																								
C	0.0019	181	6.9	0.466	0.5049	98.52%	20	0.62	1250	0.148	0.050720	2.364	0.245740	2.494	0.035140	0.339	0.444	228.11	54.60	223.11	5.00	222.64	0.74	
D	0.0036	103	3.8	0.400	0.5484	99.15%	34	0.39	2173	0.128	0.050830	1.010	0.247486	1.066	0.035312	0.195	0.371	233.15	23.30	224.53	2.15	223.71	0.43	
E	0.0022	128	4.9	0.479	0.4126	98.40%	19	0.55	1155	0.151	0.050255	2.809	0.244098	2.930	0.035227	0.436	0.347	206.82	65.14	221.77	5.84	223.18	0.96	
G	0.0027	54	2.2	0.413	0.2142	95.76%	7	0.78	435	0.131	0.050602	2.246	0.246105	2.396	0.035274	0.221	0.701	222.74	51.94	223.41	4.81	223.47	0.49	
H	0.0016	104	4.1	0.356	0.2442	96.46%	8	0.74	521	0.115	0.051633	3.585	0.251093	3.786	0.035270	0.410	0.532	269.18	82.19	227.46	7.72	223.45	0.90	

(a) A, B etc. are labels for fractions composed of single zircon grains or fragments; all fractions annealed and chemically abraded after Mattinson (2005) and Scoates and Friedman (2008).
 (b) Model Th/U ratio calculated from radiogenic ²⁰⁶Pb/²⁰⁶Pb ratio and ²⁰⁷Pb/²³⁵U age.
 (c) Pb* and Pbc represent radiogenic and common Pb, respectively; mol % ²⁰⁶Pb* with respect to radiogenic, blank and initial common Pb.
 (d) Measured ratio corrected for spike and fractionation only. Mass discrimination of 0.25‰/amu based on analysis of NBS-982; all Daily analyses.
 (e) Corrected for fractionation, spike, and common Pb; up to 0.78 pg of common Pb was assumed to be procedural blank. ²⁰⁶Pb/²⁰⁶Pb = 18.50 ± 1.0‰; ²⁰⁷Pb/²⁰⁶Pb = 15.50 ± 1.0‰;
²⁰⁸Pb/²⁰⁶Pb = 38.40 ± 1.0‰ (all uncertainties 1-sigma). Excess over blank was assigned to initial common Pb, using the Stacey and Kramers (1975) two-stage Pb isotope evolution model at 224 Ma.
 (f) Errors are 2-sigma, propagated using the algorithms of Schmitz and Schoene (2007) and Crowley et al. (2007).
 (g) Calculations are based on the decay constants of Jaffey et al. (1971). ²⁰⁶Pb/²³⁸U and ²⁰⁷Pb/²⁰⁶Pb ages corrected for initial disequilibrium in ²³⁰Th/²³⁸U using Th/U [magma] = 3.
 (h) Corrected for fractionation, spike, and blank Pb only.
 (i) Nominal fraction weights estimated from photomicrographic grain dimensions, adjusted for partial dissolution during chemical abrasion.
 (j) Nominal U and total Pb concentrations subject to uncertainty in photomicrographic estimation of weight and partial dissolution during chemical abrasion.

Table 5. U-Th-Pb analytical results for LDi07-7-2.

Sample	Compositional Parameters										Radiogenic Isotope Ratios						Isotopic Ages						
	Wt.	U	Pb	Th	²⁰⁶ Pb*	mol %	Pb*	Pb _c	Pb _c	Pb _c	²⁰⁸ Pb	²⁰⁷ Pb	²⁰⁶ Pb	corr.	²⁰⁷ Pb	²⁰⁶ Pb	²³⁵ U	²³⁸ U	²⁰⁶ Pb				
	mg	ppm	ppm	U	x10 ⁻¹³ mol	²⁰⁶ Pb*	Pb _c	(pg)	(pg)	(pg)	²⁰⁶ Pb	²⁰⁷ Pb	²⁰⁶ Pb	% err	²⁰⁶ Pb	²³⁸ U	% err	²⁰⁶ Pb	²³⁵ U	% err	²⁰⁶ Pb		
(a)	(h)	(i)	(j)	(b)	(c)	(c)	(c)	(c)	(c)	(d)	(e)	(e)	(f)	(f)	(g)	(g)	(f)	(g)	(f)	(g)	(f)	(g)	(f)
LDi07-7-2																							
A	0.002	70	2.8	0.272	0.1669	96.33%	7	0.52	504	0.086	0.050145	1.554	0.245405	1.651	0.035494	0.191	0.551	201.73	36.07	222.84	3.30	224.84	0.42
E	0.001	343	12.5	0.274	0.4553	98.59%	20	0.54	1308	0.087	0.050436	0.737	0.246039	0.795	0.035381	0.128	0.516	215.12	17.06	223.35	1.59	224.14	0.28
H	0.001	102	4.2	0.234	0.1516	94.95%	5	0.66	367	0.073	0.049914	2.200	0.244417	2.337	0.035515	0.216	0.663	190.99	51.17	222.03	4.66	224.97	0.48
K	0.001	84	3.5	0.271	0.0992	94.51%	5	0.47	337	0.085	0.050094	2.922	0.244127	3.096	0.035345	0.330	0.567	199.35	67.85	221.79	6.17	223.92	0.73

(a) A, B etc. are labels for fractions composed of single zircon grains or fragments; all fractions annealed and chemically abraded after Mattinson (2005) and Scoates and Friedman (2008).
 (b) Model Th/U ratio calculated from radiogenic ²⁰⁶Pb/²⁰⁶Pb ratio and ²⁰⁷Pb/²³⁵U age.
 (c) Pb* and Pbc represent radiogenic and common Pb, respectively; mol % ²⁰⁶Pb* with respect to radiogenic, blank and initial common Pb.
 (d) Measured ratio corrected for spike and fractionation only. Mass discrimination of 0.25‰/amu based on analysis of NBS-982; all Daily analyses.
 (e) Corrected for fractionation, spike, and common Pb; all common Pb was assumed to be procedural blank. ²⁰⁶Pb/²⁰⁶Pb = 18.50 ± 1.0‰; ²⁰⁷Pb/²⁰⁶Pb = 15.50 ± 1.0‰;
²⁰⁸Pb/²⁰⁶Pb = 38.40 ± 1.0‰ (all uncertainties 1-sigma).
 (f) Errors are 2-sigma, propagated using the algorithms of Schmitz and Schoene (2007) and Crowley et al. (2007).
 (g) Calculations are based on the decay constants of Jaffey et al. (1971). ²⁰⁶Pb/²³⁸U and ²⁰⁷Pb/²⁰⁶Pb ages corrected for initial disequilibrium in ²³⁰Th/²³⁸U using Th/U [magma] = 3.
 (h) Nominal fraction weights estimated from photomicrographic grain dimensions, adjusted for partial dissolution during chemical abrasion.
 (i) Nominal U and total Pb concentrations subject to uncertainty in photomicrographic estimation of weight and partial dissolution during chemical abrasion.

Table 7. U-Th-Pb analytical results for MM14-50-2.

Sample	Compositional Parameters				Radiogenic Isotope Ratios								Isotopic Ages										
	Wt.	U	Pb	Th	Pb _c	Pb _c	²⁰⁶ Pb/ ²⁰⁸ Pb	²⁰⁷ Pb/ ²⁰⁶ Pb	²⁰⁷ Pb/ ²³⁵ U	²⁰⁶ Pb/ ²³⁵ U	corr.	²⁰⁷ Pb/ ²⁰⁶ Pb	²⁰⁷ Pb/ ²³⁵ U	²⁰⁶ Pb/ ²³⁸ U	±								
	mg	ppm	ppm	U	(pg)	Pb _c	x 10 ⁻¹³ mol ²⁰⁶ Pb* mol %	mol %	% err	% err	% err	% err	±	±	±								
(a)	(i)	(j)	(b)	(c)	(c)	(c)	(c)	(d)	(e)	(e)	(f)	(f)	(g)	(f)	(g)	(f)							
MM14-50-2																							
A	0.0020	92	3.6	0.382	0.2619	96.34%	8	0.81	505	0.123	0.051014	1.689	0.241254	1.770	0.034299	0.191	0.469	241.45	38.92	219.45	3.49	217.40	0.41
B	0.0020	1220	47.7	0.730	3.5815	99.80%	164	0.58	9420	0.232	0.050662	0.127	0.245984	0.290	0.035214	0.213	0.917	225.50	2.93	223.31	0.58	223.10	0.47
C	0.0016	94	3.6	0.364	0.2220	97.80%	13	0.41	841	0.116	0.050688	0.807	0.246643	0.893	0.035291	0.169	0.576	226.67	18.65	223.85	1.79	223.58	0.37
E	0.0008	572	22.5	0.530	0.6720	98.06%	15	1.09	954	0.168	0.050557	0.636	0.245617	0.714	0.035235	0.149	0.601	220.67	14.70	223.01	1.43	223.23	0.33

(a) A, B etc. are labels for fractions composed of single zircon grains or fragments; all fractions annealed and chemically abraded a fler Mattinson (2005) and Scoates and Friedman (2008).
 (b) Model Th/U ratio calculated from radiogenic ²⁰⁶Pb/²⁰⁶Pb ratio and ²⁰⁷Pb/²³⁵U age.
 (c) Pb_c* and Pb_c represent radiogenic and common Pb, respectively; mol % ²⁰⁶Pb* with respect to radiogenic, blank and initial common Pb.
 (d) Measured ratio corrected for spike and fractionation only. Mass discrimination of 0.30% ± 0.05%/amu based on analysis of NBS-982; all Daily analyses.
 (e) Corrected for fractionation, spike, and common Pb; up to 1 pg common Pb was assumed to be procedural blank: ²⁰⁶Pb/²⁰⁶Pb = 18.50 ± 1.0%; ²⁰⁷Pb/²⁰⁶Pb = 15.50 ± 1.0%; ²⁰⁶Pb/²⁰⁴Pb = 38.40 ± 1.0% (1σ errors).
 Excess over blank was assigned to initial common Pb, using the Stacey and Kramers (1975) two-stage Pb isotope evolution model at 223 Ma.
 (f) Errors are 2-sigma, propagated using the algorithms of Schmitz and Schoene (2007) and Crowley et al. (2007).
 (g) Calculations are based on the decay constants of Jarley et al. (1971). ²⁰⁶Pb/²³⁸U and ²⁰⁷Pb/²³⁵U ages corrected for initial disequilibrium in ²³⁰Th/²³⁸U using Th/U [magma] = 3.
 (h) Corrected for fractionation, spike, and blank Pb only.
 (i) Nominal fraction weights estimated from photomicrographic grain dimensions, adjusted for partial dissolution during chemical abrasion.
 (j) Nominal U and total Pb concentrations subject to uncertainty in photomicrographic estimation of weight and partial dissolution during chemical abrasion.

Table 8. Argon analytical results for LD107-20-3.

Laser	Isotope Ratios										K/Cu	Rho	σ	2σ	³⁹ Ar/ ⁴⁰ Ar	2s	³⁶ Ar/ ³⁹ Ar	2σ	σ	2σ	f ⁴⁰ Ar rad	⁴⁰ Ar*/ ³⁹ Ar	K Age ± 2σ
	⁴⁰ Ar/ ³⁹ Ar	2σ	³⁶ Ar/ ⁴⁰ Ar	2σ	³⁶ Ar/ ⁴⁰ Ar	2σ	³⁹ Ar/ ⁴⁰ Ar	2σ	³⁶ Ar/ ⁴⁰ Ar	2σ													
2.00	172.99	2.72	0.58	0.02	0.01	0.00	0.00	0.00	0.00	0.00	0.009	0.78	0.00	0.00	0.21	0.11	0.358	0.358	0.358	0.358	3.37 ± 43.42		
2.30	27.56	0.34	0.07	0.00	0.04	0.00	0.00	0.00	0.00	0.00	0.002	2.09	0.00	0.00	22.54	0.76	6.214	6.214	6.214	6.214	57.61 ± 6.98		
2.60	23.49	0.15	0.02	0.00	0.04	0.00	0.00	0.00	0.00	0.00	0.007	10.66	0.00	0.00	79.54	6.32	18.687	18.687	18.687	18.687	167.97 ± 1.71		
2.90	23.50	0.15	0.00	0.00	0.04	0.00	0.00	0.00	0.00	0.00	0.001	25.02	0.00	0.00	95.70	12.09	22.487	22.487	22.487	22.487	200.30 ± 1.23		
3.10	24.20	0.13	0.00	0.00	0.04	0.00	0.00	0.00	0.00	0.00	0.002	31.99	0.00	0.00	97.35	10.11	23.561	23.561	23.561	23.561	209.33 ± 1.51		
3.20	24.31	0.16	0.00	0.00	0.04	0.00	0.00	0.00	0.00	0.00	0.000	30.25	0.00	0.00	96.84	9.37	23.546	23.546	23.546	23.546	209.20 ± 1.83		
3.30	24.59	0.13	0.00	0.00	0.04	0.00	0.00	0.00	0.00	0.00	0.001	24.18	0.00	0.00	96.03	3.61	23.614	23.614	23.614	23.614	209.78 ± 2.95		
3.40	24.47	0.12	0.00	0.00	0.04	0.00	0.00	0.00	0.00	0.00	0.001	24.82	0.00	0.00	97.22	7.19	23.787	23.787	23.787	23.787	211.22 ± 1.52		
3.50	24.45	0.11	0.00	0.00	0.04	0.00	0.00	0.00	0.00	0.00	0.000	20.49	0.00	0.00	97.08	6.84	23.734	23.734	23.734	23.734	210.78 ± 2.08		
3.60	24.45	0.10	0.00	0.00	0.04	0.00	0.00	0.00	0.00	0.00	0.001	17.92	0.00	0.00	97.24	5.47	23.777	23.777	23.777	23.777	211.14 ± 1.79		
3.80	24.09	0.15	0.00	0.00	0.04	0.00	0.00	0.00	0.00	0.00	0.000	15.76	0.00	0.00	98.03	12.67	23.613	23.613	23.613	23.613	209.76 ± 1.80		
4.00	24.12	0.16	0.00	0.00	0.04	0.00	0.00	0.00	0.00	0.00	0.000	12.76	0.00	0.00	98.26	6.81	23.698	23.698	23.698	23.698	210.47 ± 1.56		
4.30	24.03	0.16	0.00	0.00	0.04	0.00	0.00	0.00	0.00	0.00	0.000	11.77	0.00	0.00	98.44	9.45	23.655	23.655	23.655	23.655	210.12 ± 1.44		
4.60	23.91	0.15	0.00	0.00	0.04	0.00	0.00	0.00	0.00	0.00	0.000	10.63	0.00	0.00	99.14	9.20	23.703	23.703	23.703	23.703	210.52 ± 1.37		

Analysis by Janet Gabites, Pacific Centre for Isotopic and Geochemical Research

- J = 0.00522800 ± 0.00000784 Volume 39A 1.779 x E-13 cm³ NPT
- Integrated Date = 204.98 ± 0.47 Ma
 Plateau age = 210.27 ± 0.68 Ma(2s, including J-error of . MSWD = 0.70, probability=0.71 Includes 80.7% of the 3steps 5 through 14
 Inverse isochron (correlation age) results, plateau steps: Model 1 Solution (±95% conf.) on 10 points
 07LDI-20.3 Biotite age = 210.5 ± 1.3 Ma Initial ⁴⁰Ar/³⁹Ar=441 ± 120 MSWD = 1.4 Probability = 0.19

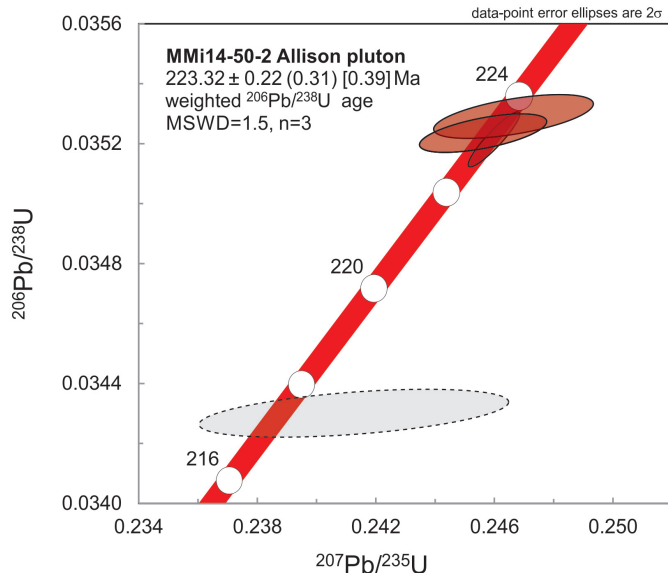


Fig. 14. U-Pb concordia diagram showing TIMS zircon U-Pb age results from sample MMI14-50-2 of the Allison pluton. Weighted age 223.32 ± 0.22 Ma based on $^{206}\text{Pb}/^{238}\text{U}$ ages of 4 grains. Concordia bands include 2σ errors of U decay constants.

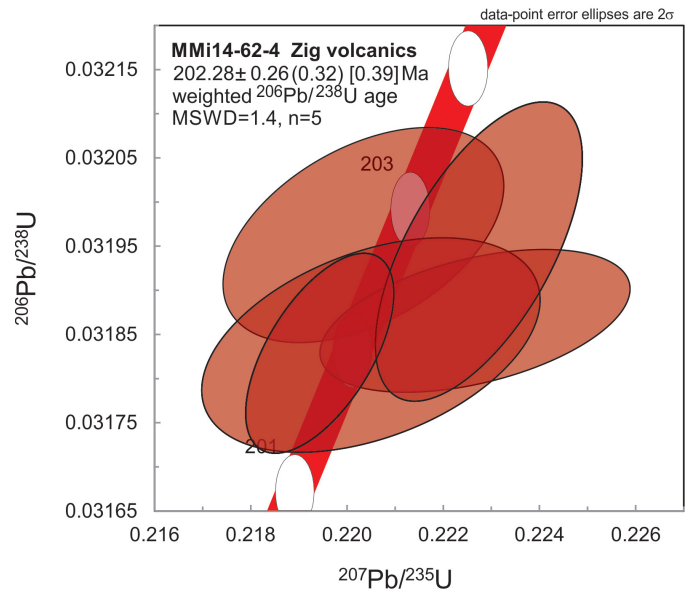


Fig. 16. U-Pb concordia diagram showing TIMS zircon U-Pb age results from sample MMI14-62-4, sparsely quartz-phyric andesite tuff, correlated with host rocks near the Zig (NOR 30) mineral prospect. Weighted age 202.3 ± 0.3 Ma based on $^{206}\text{Pb}/^{238}\text{U}$ ages of 5 grains. Concordia bands include 2σ errors of U decay constants.

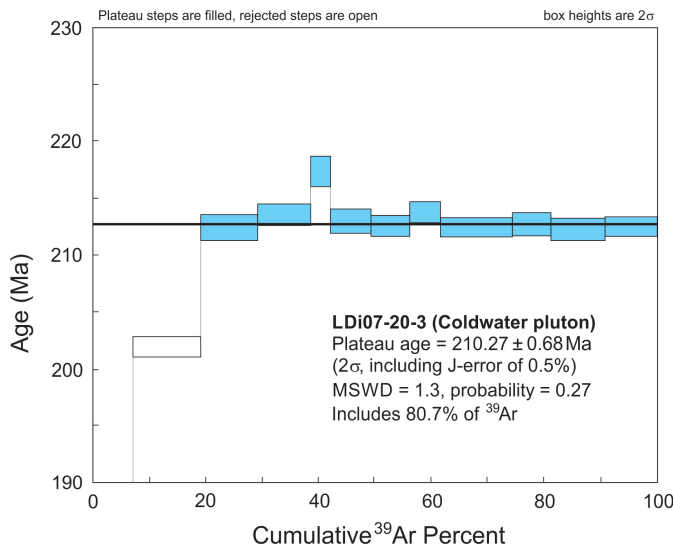


Fig. 15. $^{40}\text{Ar}/^{39}\text{Ar}$ step heating gas release spectra from sample LDi07-20-3, a biotite separate from quartz-diorite near the centre of the Coldwater pluton. A plateau age of 210.27 ± 0.68 Ma dates crystallization of the pluton and time of emplacement into upper stratified rocks of the Western belt.

but no good bedding or sedimentary sorting could be detected.

Based on a weighted mean $^{206}\text{Pb}/^{238}\text{U}$ date for 5 concordant and overlapping single zircon grains, the Zig andesite is 202.3 ± 0.3 Ma (Fig. 16, Table 9), considerably younger than the 215 Ma Re-Os chalcocite age. Three explanations should be considered: 1) the unit spans an age of nearly 13 m.y.; 2) one of the ages is in error; or 3) Zig unit has been reworked and mixed with a younger tuffaceous component which included the most attractive zircons for analysis. While we consider the third option as the most likely, U-Pb analysis of the Zig

unit at NOR30, and a analysis of a broader selection of zircon morphologies from sample MMI14-62-4 will be required to resolve this problem.

3.2.1.9. Sample MMI14-19-3 (U12), western Pennask batholith, gabbro from border phase; 193.1 ± 0.2 Ma

Interior portions of the Pennask batholith tend to be homogeneous and isotropic, white-weathering, medium- to coarse-grained hornblende-biotite granodiorite to tonalite (see descriptions in Mihalynuk et al., 2015). However, near its southwest margin, the batholith is highly variable in composition, ranging from granodiorite to varitextured, locally pegmatitic, hornblende gabbro (Fig. 17).

The gabbro contains 30-70% hornblende, with intragranular plagioclase comprising most of the remainder of the rock. In places, plagioclase is intergrown with pink perthitic K-feldspar; both have been moderately to strongly epidote altered. Fine- to medium-grained magnetite comprises $\sim 10\%$, and also comprises $\sim 80\%$ of centimeter-thick bands. Fine-grained biotite occurs as scattered booklets and glomerocrysts ($< 2\%$). Trace titanite is fine to medium grained. Irregular voids up to 5cm across may be mirolitic cavities or possibly dissolved mineral matter. Locally, the gabbro contains up to a few percent pyrite and traces chalcocopyrite. Because some biotite and K-feldspar textures could have been produced by potassic alteration, and sulphides are locally conspicuous, we sampled the gabbro to test if isolated outcrops interpreted as Pennask border phase might be part of the Copper Mountain suite (Late Triassic), which has considerably higher mineral potential.

Mineralized gabbro sample MMI14-19-3 yielded both abundant zircon and titanite. Three zircon grains analyzed



Fig. 17. Representative outcrop of varitextured hornblende gabbro of the Pennask batholith border phase near geochronology sample site MMI14-19-3.

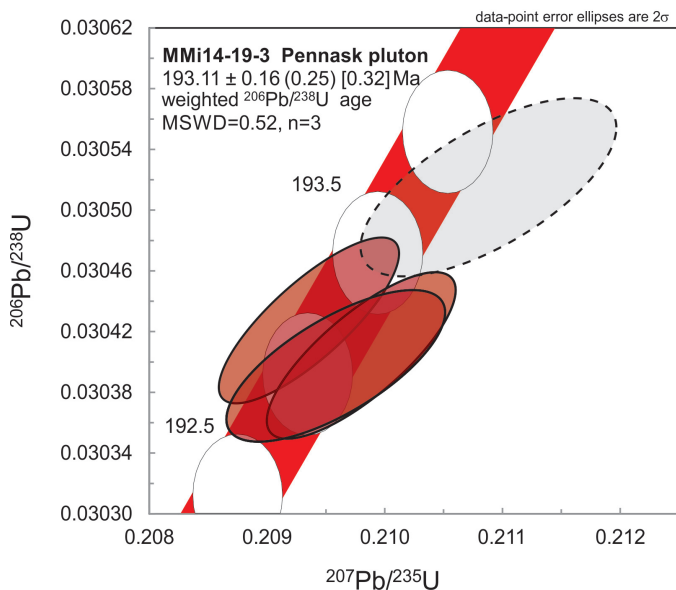


Fig. 18. U-Pb concordia diagram showing TIMS zircon (shaded) and titanite age results from sample MMI14-19-3 of undeformed Pennask batholith. Weighted age 193.1 ± 0.2 Ma based on $^{206}\text{Pb}/^{238}\text{U}$ ages of 3 zircon grains. TIMS titanite age results are slightly younger than zircon age results. Concordia bands include 2σ errors of U decay constants.

overlap concordia at 193.11 ± 0.16 Ma. Titanite from the same sample are slightly younger with a weighted $^{206}\text{Pb}/^{238}\text{U}$ date for 4 overlapping and concordant fractions yielding 192.9 ± 0.4 Ma (Fig. 18, Table 10). This age couple is consistent with rapid cooling following crystallization.

These new Early Jurassic ages confirm assignment of

the border rocks to the Pennask batholith (Mihalynuk et al., 2015) and are the same as previous crystallization ages farther northeast (194 ± 1 Ma; Parrish and Monger, 1992).

3.2.1.10. MMI14-59-12 (U13), post-Nicola rhyolite ‘Osprey volcanic unit’; 163.2 ± 0.2 Ma

In the study area north of Princeton, grey porphyritic granodiorite intrudes andesite breccia and flow banded rhyolite that strongly resembles the Pimanus Formation of the Spences Bridge Group (Early Cretaceous). Mihalynuk and Logan (2014a) included this porphyritic granodiorite with the Summers Creek suite of intrusions, thought to be ~ 99 Ma (K-Ar cooling ages of Preto, 1979; recalculated in Breitsprecher and Mortensen, 2005). However, zircons extracted from the intrusion overlap concordia between 160 Ma and 164 Ma (see Osprey Lake batholith: Sample MMI 13-4-8, Mihalynuk et al., 2015) indicating that the volcanic package is Late Jurassic or older. To test for an inherited component we analyzed the central and perimeter zones of ten zircons by laser ablation (LA-ICPMS). These analyses confirmed the TIMS results, with a weighted age for 9 of the 10 zircons at 162 ± 2 Ma. The youngest concordant grain gave a $^{206}\text{Pb}/^{238}\text{U}$ age of 160.67 ± 0.21 Ma, which we take as a maximum crystallization age for the intrusion, given that the grains were chemically abraded.

Sample MMI14-59-12 was collected from the rhyolite unit as far from the intrusive contact as possible without losing outcrop continuity (Fig. 2). Five zircon grains gave results that overlap concordia to give a weighted $^{206}\text{Pb}/^{238}\text{U}$ age of 163.22 ± 0.15 Ma (Fig. 19, Table 11). Not only is this age consistent with the geological requirement that it be older than

Table 9. U-Th-Pb analytical results for MM114-62-4.

Sample	Compositional Parameters				Radiogenic Isotope Ratios						Isotopic Ages						
	U ppm	Pb ppm	Th/U	$^{206}\text{Pb}^*/^{206}\text{Pb}$ mol %	Pb*/Pb _c (pg)	$^{206}\text{Pb}/^{206}\text{Pb}$	$^{207}\text{Pb}/^{206}\text{Pb}$	$^{207}\text{Pb}/^{235}\text{U}$	% err	$^{206}\text{Pb}/^{238}\text{U}$	% err	corr. $^{207}\text{Pb}/^{235}\text{U}$	% err	$^{206}\text{Pb}/^{238}\text{U}$	% err		
(a)	(i)	(j)	(b)	(c)	(c)	(c)	(d)	(e)	(f)	(e)	(f)	(e)	(f)	(g)	(f)	(g)	(f)
MM114-62-4																	
A	0.0115	39	1.4	0.394	0.5933	97.64%	12	1.18	782	0.124	0.049774	0.926	0.219353	1.036	0.031962	0.312	0.482
B	0.0056	56	2.1	0.452	0.4172	95.99%	7	1.44	460	0.144	0.050361	1.010	0.221264	1.096	0.031865	0.208	0.495
C	0.0071	53	2.3	0.321	0.4972	90.75%	3	4.18	199	0.102	0.049962	1.146	0.219324	1.250	0.031838	0.312	0.445
D	0.0057	94	3.2	0.389	0.7173	98.45%	19	0.93	1191	0.124	0.050401	0.571	0.221985	0.752	0.031944	0.434	0.655
E	0.0039	194	6.6	0.432	1.0042	98.77%	24	1.03	1501	0.137	0.050000	0.462	0.219425	0.573	0.031828	0.291	0.599

(a) A, B etc. are labels for fractions composed of single zircon grains or fragments; all fractions annealed and chemically abraded after Mattinson (2005) and Scoates and Friedman (2008).

(b) Model Th/U ratio calculated from radiogenic $^{206}\text{Pb}/^{206}\text{Pb}$ ratio and $^{207}\text{Pb}/^{235}\text{U}$ age.

(c) Pb* and Pb_c represent radiogenic and common Pb, respectively; mol % $^{206}\text{Pb}^*$ with respect to radiogenic, blank and initial common Pb.

(d) Measured ratio corrected for spike and fractionation only. Mass discrimination of 0.30% ± 0.05% amu based on analysis of NBS-982; all Daly analyses.

(e) Corrected for fractionation, spike, and common Pb; up to 1 pg common Pb was assumed to be procedural blank: $^{206}\text{Pb}/^{206}\text{Pb} = 18.50 \pm 1.0\%$; $^{207}\text{Pb}/^{206}\text{Pb} = 38.40 \pm 1.0\%$ (1σ errors).

(f) Excess over blank was assigned to initial common Pb, using the Stacey and Kramers (1975) two-stage Pb isotope evolution model at 202 Ma.

(g) Errors are 2-sigma, propagated using the algorithms of Schmitz and Schoene (2007) and Crowley et al. (2007).

(h) Calculations are based on the decay constants of Jaffey et al. (1971). $^{206}\text{Pb}/^{238}\text{U}$ and $^{207}\text{Pb}/^{235}\text{U}$ ages corrected for initial disequilibrium in $^{230}\text{Th}/^{238}\text{U}$ using Th/U [magma] = 3.

(i) Corrected for fractionation, spike, and blank Pb only.

(j) Nominal fraction weights estimated from photomicrographic grain dimensions, adjusted for partial dissolution during chemical abrasion.

(k) Nominal U and total Pb concentrations subject to uncertainty in photomicrographic estimation of weight and partial dissolution during chemical abrasion.

Table 10. U-Th-Pb analytical results for MM114-19-3.

Sample	Compositional Parameters				Radiogenic Isotope Ratios						Isotopic Ages						
	U ppm	Pb ppm	Th/U	$^{206}\text{Pb}^*/^{206}\text{Pb}$ mol %	Pb*/Pb _c (pg)	$^{206}\text{Pb}/^{206}\text{Pb}$	$^{207}\text{Pb}/^{206}\text{Pb}$	$^{207}\text{Pb}/^{235}\text{U}$	% err	$^{206}\text{Pb}/^{238}\text{U}$	% err	corr. $^{207}\text{Pb}/^{235}\text{U}$	% err	$^{206}\text{Pb}/^{238}\text{U}$	% err		
(a)	(i)	(j)	(b)	(c)	(c)	(c)	(d)	(e)	(f)	(e)	(f)	(e)	(f)	(g)	(f)	(g)	(f)
MM114-19-3																	
B	0.0040	465	15.4	0.619	2.3578	99.52%	65	0.94	3842	0.197	0.049902	0.200	0.209352	0.299	0.030427	0.147	0.807
C	0.0025	603	20.4	0.693	1.9114	99.50%	63	0.79	3677	0.221	0.050046	0.217	0.209797	0.313	0.030404	0.148	0.784
D	0.0029	282	9.3	0.550	1.0388	99.20%	38	0.69	2314	0.175	0.050121	0.337	0.210879	0.421	0.030515	0.157	0.671
E	0.0025	343	11.4	0.608	1.0866	99.42%	53	0.53	3182	0.194	0.050005	0.284	0.209580	0.363	0.030397	0.134	0.705
T2	0.0413	18	1.4	1.590	0.9370	73.06%	1	28.46	68	0.508	0.050200	3.736	0.209424	3.862	0.030257	0.540	0.298
T3	0.0522	39	2.3	1.411	2.5914	84.47%	2	39.26	119	0.447	0.049762	1.650	0.208185	1.743	0.030342	0.302	0.384
T4	0.0370	50	3.2	1.377	2.3583	80.91%	2	45.88	96	0.439	0.050124	1.921	0.210606	2.014	0.030473	0.378	0.335
T5	0.0435	17	1.7	2.425	0.9474	66.70%	1	38.99	55	0.773	0.050040	4.304	0.209310	4.433	0.030337	0.742	0.254

(a) A, B etc. are labels for fractions composed of single zircon grains or fragments; all fractions annealed and chemically abraded after Mattinson (2005) and Scoates and Friedman (2008).

(b) Model Th/U ratio calculated from radiogenic $^{206}\text{Pb}/^{206}\text{Pb}$ ratio and $^{207}\text{Pb}/^{235}\text{U}$ age.

(c) Pb* and Pb_c represent radiogenic and common Pb, respectively; mol % $^{206}\text{Pb}^*$ with respect to radiogenic, blank and initial common Pb.

(d) Measured ratio corrected for spike and fractionation only. Mass discrimination of 0.30% ± 0.05% amu based on analysis of NBS-982; all Daly analyses.

(e) Corrected for fractionation, spike, and common Pb; up to 1 pg common Pb was assumed to be procedural blank: $^{206}\text{Pb}/^{206}\text{Pb} = 18.50 \pm 1.0\%$; $^{207}\text{Pb}/^{206}\text{Pb} = 38.40 \pm 1.0\%$ (1σ errors).

(f) Excess over blank was assigned to initial common Pb, using the Stacey and Kramers (1975) two-stage Pb isotope evolution model at 193 Ma.

(g) Errors are 2-sigma, propagated using the algorithms of Schmitz and Schoene (2007) and Crowley et al. (2007).

(h) Calculations are based on the decay constants of Jaffey et al. (1971). $^{206}\text{Pb}/^{238}\text{U}$ and $^{207}\text{Pb}/^{235}\text{U}$ ages corrected for initial disequilibrium in $^{230}\text{Th}/^{238}\text{U}$ using Th/U [magma] = 3.

(i) Corrected for fractionation, spike, and blank Pb only.

(j) Nominal fraction weights estimated from photomicrographic grain dimensions, adjusted for partial dissolution during chemical abrasion.

(k) Nominal U and total Pb concentrations subject to uncertainty in photomicrographic estimation of weight and partial dissolution during chemical abrasion.

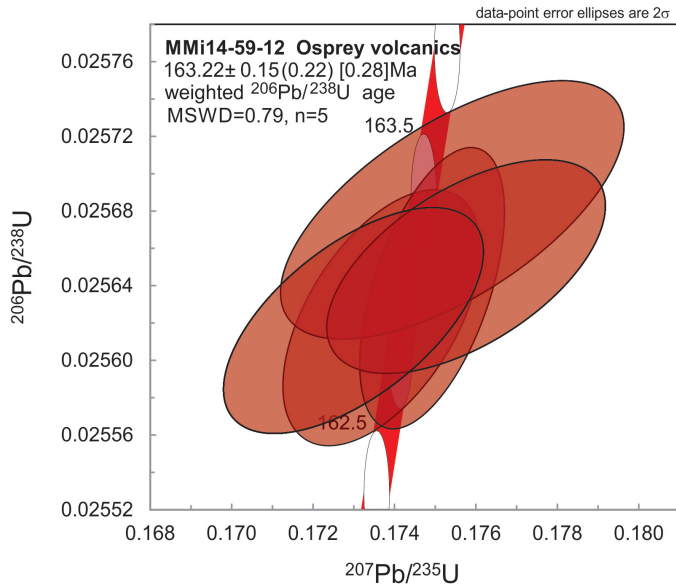


Fig. 19. U-Pb concordia diagram showing TIMS zircon U-Pb age results from sample MMI14-59-12, from rhyolite in a newly-defined volcanic unit, comagmatic with the Osprey batholith. Weighted age 163.2 ± 0.2 Ma based on $^{206}\text{Pb}/^{238}\text{U}$ ages of 5 grains. Concordia bands include 2σ errors of U decay constants.

the crosscutting 162 ± 2 Ma (or 160.7 ± 0.2 Ma based on the youngest concordant grain) granodiorite, but it strongly hints of an intrusion that cuts its comagmatic volcanic carapice. This is the first example of demonstrable Late Jurassic volcanic rocks presumably overlying older Nicola arc strata in the study area.

We include the granodiorite with the Osprey Lake batholith; a younger phase than the most widespread and distinctive K-feldspar megacrystic granite phase dated at 166 ± 1 Ma (U-Pb zircon; Parrish and Monger, 1992). We introduce the informal name 'Osprey volcanic unit' for the comagmatic andesite and rhyolite rocks cross cut by the batholith which, despite a lithologic similarity, are unrelated to the Pimanus Formation.

3.2.1.11. Sample MMI14-53-2 (U14), Snowstorm quartz-feldspar porphyry; 53.36 ± 0.07 Ma

Base metal sulphide vein mineralization at the Snowstorm prospect is developed in yellow and rust-weathering, coarse quartz-eye feldspar porphyry of the 'Otter intrusions'. Disseminated fine cubes of pyrite (~1-2%) are widespread and clay-alteration is pervasive. Where least altered, phenocrysts of orthoclase (up to 1 cm across and 15-20%) and hornblende (medium to coarse-grained, up to 15%) are visible but largely replaced by clay minerals and chlorite-?pyrophyllite. Coarse quartz phenocrysts (~25%) are little affected by alteration.

Limited production of gold, silver and lead from tracked adits at the Snowstorm property date from 1917 to 1927 (Groves, 1989). At least two adits were drifted along mineralized zones. Analysis of mineralized quartz stockwork veining revealed >1% zinc and, in one grab sample, 22.7 ppm indium (Mihalynuk et al., 2015). Although the mineralization has been

classified as shear-related veining (MINFILE 092HNE032), open space quartz stockworks and shallow intrusive host rocks are more consistent with intrusion-related vein mineralization. If related to the quartz-eye feldspar porphyry host intrusion, a crystallization age would provide an approximate age for mineralization (or maximum age for shear-related veining). Sample MMI14-53-2, collected at creek level and upstream of the two major adits, returned a U-Pb zircon crystallization age of 53.36 ± 0.07 Ma from three grains that overlap concordia (Fig. 20, Table 12). The age is consistent with K-Ar cooling ages from other quartz-feldspar porphyry dikes and stocks that cluster ~53 Ma, including some associated with gold mineralization at the Siwash mine (Armstrong and Petö, 1981 and Hunt and Roddick, 1990; recalculated in Breitsprecher and Mortensen, 2005).

3.2.2. LA-ICPMS detrital zircon ages

3.2.2.1. Sample MMI14-23-15 (D9), Nicola Group, Central belt, Ketcham rhyolite sharpstone conglomerate (<239 Ma, possibly <227 Ma)

Between Missezula Lake and Missezula Mountain (Fig. 2), well-bedded sandstone, conglomerate (containing angular clasts of aphanitic to feldspar- and quartz-phyric rhyolite, Fig. 21), and lesser argillite up to tens of metres thick, are interlayered with reworked ash and lesser lapilli tuff. Because felsic rocks are atypical of the Central belt, Mihalynuk et al. (2014) speculated on possible correlatives including the Skwel Pecken Formation (Early to Middle Jurassic) as defined near Hedley (Ray and Dawson, 1994) or a lithologically similar Nicola unit at Coalmont.

A sample was collected from the north of the Ketchan copper

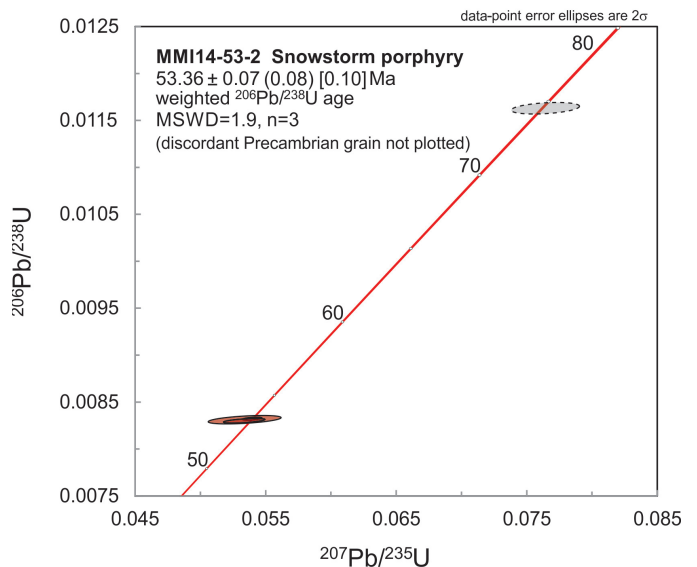


Fig. 20. U-Pb concordia diagram showing TIMS zircon U-Pb age results from sample MMI14-53-2, altered quartz-feldspar porphyry intrusion at the old Snowstorm mine. Weighted age 53.36 ± 0.07 Ma based on $^{206}\text{Pb}/^{238}\text{U}$ ages of 3 grains. Concordia bands include 2σ errors of U decay constants.

Table 11. U-Th-Pb analytical results for MM114-59-12 Osprey.

Sample	Compositional Parameters				Radiogenic Isotope Ratios						Isotopic Ages												
	Wt. mg	U ppm	Pb ppm	$\frac{Th}{U}$	$\frac{^{206}Pb}{^{208}Pb}$	mol % $^{206}Pb^*$	$\frac{Pb^*}{Pb_c}$	$\frac{^{206}Pb}{^{208}Pb}$	$\frac{^{207}Pb}{^{206}Pb}$	$\frac{^{207}Pb}{^{235}U}$	% err	$\frac{^{206}Pb}{^{238}U}$	corr. coef.	$\frac{^{207}Pb}{^{206}Pb}$	$\frac{^{207}Pb}{^{235}U}$	$\frac{^{206}Pb}{^{238}U}$	% err						
(a)	(i)	(j)	(i)	(b)	(c)	(c)	(c)	(d)	(e)	(e)	(f)	(e)	(f)	(g)	(g)	(f)	(g)	(f)					
MM114-59-12																							
A	0.0020	157	4.3	0.293	0.3351	97.25%	10	0.78	0.093	0.049160	1.041	0.173675	1.141	0.025623	0.219	0.535	155.47	24.36	162.60	1.71	163.09	0.35	
B	0.0021	159	4.3	0.359	0.3562	98.10%	15	0.57	0.775	0.049481	0.730	0.174918	0.831	0.025639	0.240	0.539	170.69	17.05	163.68	1.26	163.19	0.39	
C	0.0013	129	3.8	0.257	0.1789	94.91%	5	0.79	3.63	0.082	0.049539	1.832	0.175411	1.966	0.025681	0.221	0.640	173.44	42.75	164.10	2.98	163.46	0.36
D	0.0015	168	5.0	0.440	0.2691	96.42%	8	0.83	5.17	0.141	0.049694	1.495	0.175752	1.592	0.025650	0.183	0.570	180.73	34.84	164.40	2.42	163.27	0.29
E	0.0015	162	4.5	0.285	0.2602	96.96%	9	0.67	6.08	0.090	0.048967	1.399	0.172982	1.508	0.025621	0.193	0.609	146.24	32.80	162.00	2.26	163.08	0.31

(a) A, B etc. are labels for fractions composed of single zircon grains or fragments; all fractions annealed and chemically abraded after Mattinson (2005) and Scoates and Friedman (2008).
 (b) Model Th/U ratio calculated from radiogenic $^{206}Pb/^{206}Pb$ ratio and $^{207}Pb/^{235}U$ age.
 (c) Pb^* and Pb_c represent radiogenic and common Pb, respectively; mol % $^{206}Pb^*$ with respect to radiogenic, blank and initial common Pb.
 (d) Measured ratio corrected for spike and fractionation only. Mass discrimination of 0.30% \pm 0.05%/amu based on analysis of NBS-982; all Daily analyses.
 (e) Corrected for fractionation, spike, and common Pb; up to 1 pg common Pb was assumed to be procedural blank; $^{206}Pb/^{206}Pb = 18.50 \pm 1.0\%$; $^{207}Pb/^{206}Pb = 15.50 \pm 1.0\%$; $^{208}Pb/^{206}Pb = 38.40 \pm 1.0\%$ (1 σ errors).
 Excess over blank was assigned to initial common Pb, using the Stacey and Kramers (1975) two-stage Pb isotope evolution model at 163 Ma.
 (f) Errors are 2-sigma, propagated using the algorithms of Schmitz and Schoene (2007) and Crowley et al. (2007).
 (g) Calculations are based on the decay constants of Jaffey et al. (1971). $^{206}Pb/^{238}U$ and $^{207}Pb/^{235}U$ ages corrected for initial disequilibrium in $^{230}Th/^{238}U$ using $Th/U [magma] = 3$.
 (h) Corrected for fractionation, spike, and blank Pb only.
 (i) Nominal fraction weights estimated from photomicrographic grain dimensions, adjusted for partial dissolution during chemical abrasion.
 (j) Nominal U and total Pb concentrations subject to uncertainty in photomicrographic estimation of weight and partial dissolution during chemical abrasion.

Table 12. U-Th-Pb analytical results for MM114-54-4 Snowstorm.

Sample	Compositional Parameters				Radiogenic Isotope Ratios						Isotopic Ages												
	Wt. mg	U ppm	Pb ppm	$\frac{Th}{U}$	$\frac{^{206}Pb}{^{208}Pb}$	mol % $^{206}Pb^*$	$\frac{Pb^*}{Pb_c}$	$\frac{^{206}Pb}{^{208}Pb}$	$\frac{^{207}Pb}{^{206}Pb}$	$\frac{^{207}Pb}{^{235}U}$	% err	$\frac{^{206}Pb}{^{238}U}$	corr. coef.	$\frac{^{207}Pb}{^{206}Pb}$	$\frac{^{207}Pb}{^{235}U}$	$\frac{^{206}Pb}{^{238}U}$	% err						
(a)	(i)	(j)	(i)	(b)	(c)	(c)	(c)	(d)	(e)	(e)	(f)	(e)	(f)	(g)	(g)	(f)	(g)	(f)					
MM114-54-4																							
A	0.0034	287	53.5	0.138	7.5852	99.91%	318	0.57	20246	0.051	0.107700	0.083	2.763932	0.173	0.186127	0.127	0.890	1760.87	1.52	1345.85	1.29	1100.36	1.28
B	0.0033	682	8.2	0.352	1.0909	99.09%	32	0.82	2039	0.113	0.047651	2.678	0.076419	2.793	0.011631	0.432	0.339	81.98	63.52	74.77	2.01	74.55	0.32
C	0.0021	224	2.4	0.855	0.1625	95.59%	7	0.62	420	0.272	0.046600	4.073	0.053378	4.272	0.008308	0.442	0.491	28.79	97.59	52.80	2.20	53.33	0.23
D	0.0025	492	4.6	0.586	0.4260	97.90%	14	0.75	883	0.188	0.047044	1.075	0.053959	1.136	0.008319	0.153	0.456	51.46	25.64	53.36	0.59	53.40	0.08
E	0.0038	239	2.3	0.561	0.3137	97.01%	10	0.80	618	0.178	0.046639	2.305	0.053349	2.436	0.008296	0.241	0.582	30.79	55.19	52.77	1.25	53.26	0.13

(a) A, B etc. are labels for fractions composed of single zircon grains or fragments; all fractions annealed and chemically abraded after Mattinson (2005) and Scoates and Friedman (2008).
 (b) Model Th/U ratio calculated from radiogenic $^{206}Pb/^{206}Pb$ ratio and $^{207}Pb/^{235}U$ age.
 (c) Pb^* and Pb_c represent radiogenic and common Pb, respectively; mol % $^{206}Pb^*$ with respect to radiogenic, blank and initial common Pb.
 (d) Measured ratio corrected for spike and fractionation only. Mass discrimination of 0.30% \pm 0.05%/amu based on analysis of NBS-982; all Daily analyses.
 (e) Corrected for fractionation, spike, and common Pb; up to 1 pg common Pb was assumed to be procedural blank; $^{206}Pb/^{206}Pb = 18.50 \pm 1.0\%$; $^{207}Pb/^{206}Pb = 15.50 \pm 1.0\%$; $^{208}Pb/^{206}Pb = 38.40 \pm 1.0\%$ (1 σ errors).
 Excess over blank was assigned to initial common Pb, using the Stacey and Kramers (1975) two-stage Pb isotope evolution model at 53 Ma.
 (f) Errors are 2-sigma, propagated using the algorithms of Schmitz and Schoene (2007) and Crowley et al. (2007).
 (g) Calculations are based on the decay constants of Jaffey et al. (1971). $^{206}Pb/^{238}U$ and $^{207}Pb/^{235}U$ ages corrected for initial disequilibrium in $^{230}Th/^{238}U$ using $Th/U [magma] = 3$.
 (h) Corrected for fractionation, spike, and blank Pb only.
 (i) Nominal fraction weights estimated from photomicrographic grain dimensions, adjusted for partial dissolution during chemical abrasion.
 (j) Nominal U and total Pb concentrations subject to uncertainty in photomicrographic estimation of weight and partial dissolution during chemical abrasion.

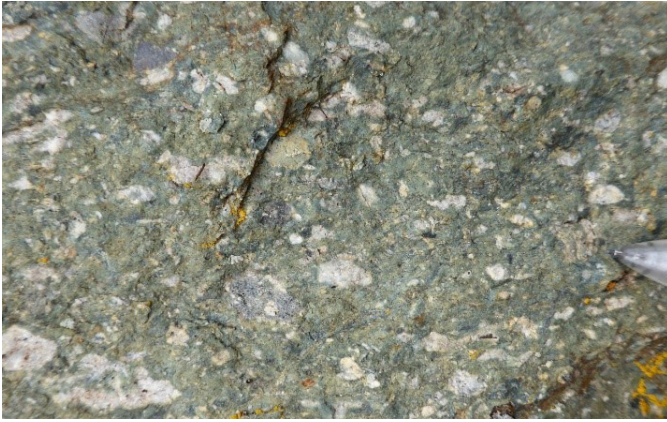


Fig. 21. Ketcham conglomerate adjacent to the Ketcham stock, with angular to subrounded clasts of aphanitic to feldspar- and quartz-phyric rhyolite (altered with epidote and chlorite). These conglomerates are some of the oldest dated rocks in the Nicola Group.

porphyry prospect, selecting from the coarsest, quartz-rich sandstone matrix (note that the Ketchan prospect is near Ketchan Creek and Ketcham Lake, we used these geographic places to name for the important conglomeratic unit). Zircons recovered were very fine-grained, but 56 grains were sufficiently large that a 15mm spot size could be analyzed. Zircons dated have a distribution peak at 239 Ma, with a sparse older population at ~255 Ma and a younger shoulder to the age distribution at ~227 Ma (Fig. 22). One orphan grain gave a $^{206}\text{Pb}/^{238}\text{U}$ age of 217 ± 8.5 Ma, but a significantly different $^{207}\text{Pb}/^{235}\text{U}$ age of 256 ± 20 Ma (see Friedman et al., 2016). Given this analytical variability, the fine grain size, and proximity of the cross-cutting Ketchan diorite body, there is a real possibility of post-depositional lead-loss causing an erroneously young age. We consider ~227 Ma

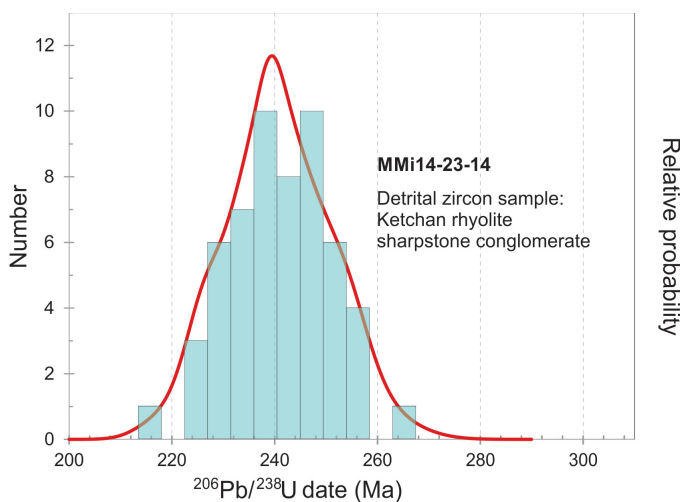


Fig. 22. Probability density plot for sample MMI14-23-15, Ketcham rhyolite clast-bearing conglomerate. A conservative maximum depositional age can be interpreted from the peak shoulder as ~227 Ma, from a protolith that is mainly ~239 Ma, but may range to 255 Ma.

the likely maximum age of the sandstone matrix, and that it was mainly sourced from felsic bodies formed at ~239 Ma, such as the 238.15 ± 0.33 Ma rhyolite tuff from nearby Missezula Mountain (sample MMI13-30-4, Mihalynuk et al., 2015; Fig. 2) and coeval rhyolite tuffite at Coalmont (238.6 ± 0.3 Ma, sample MMI14-53-13, see above).

3.2.2.2. Sample LDI14-60-3 (D10), Nicola Group, Central belt, Voght sandstone, Harmon succession <220 Ma, probably <213 Ma

Sample LDI14-60-3 is an oxidized reddish brown sandstone with granulestone layers (Fig. 23) that encloses, and is interbedded with, the Voght unit flows (Mihalynuk et al., 2015) positioned between an underlying basal polymictic conglomerate unit (Harmon conglomerate), and an overlying sequence of distinctive bladed basalt flows (Figs. 2, 3). Assuming consistent bed orientation, about 150m of covered section separates the sample site from the lowest coarse bladed feldspar porphyry flow which, together with interbedded maroon sandstone, characterize the Voght unit.

We previously correlated the Voght sandstone with other exposures of maroon sandstone and matrix-supported polymictic



Fig. 23. Maroon sandstone and granule conglomerate sampled for detrital zircons from an interval between conglomerate at the base of the Harmon succession and overlying coarsely bladed plagioclase porphyritic basalt in the Voght unit.

conglomerate ~3 km along strike to the northeast near Corbett Lake (sample 12JLO51-4), and ~8 km across strike to the east (sample MMI13-16-5; Mihalynuk et al., 2015). These were correlated with the upper and lower parts of the Voght unit. Only twenty zircons were recovered and analyzed from each sample, but they fell into strong populations with maximum depositional ages of 208 ± 4 Ma and 202 ± 4 Ma. Consistency of the younger age with a cross-cutting dike dated at $201 +0.3/-0.4$ Ma (Mihalynuk et al., 2015) supports the interpreted age of the top of the section of ~202 Ma. Our expectation was that dating zircons from the base of the Voght flows would help constrain the flow age and confirm correlation with strata to the north.

Sixty-five grains were analyzed. Disregarding the youngest orphan grain at 206 Ma (Fig. 24) five grains with 2σ errors less than 5% of the zircon age determination, and with $^{207}\text{Pb}/^{235}\text{U}$ and $^{206}\text{Pb}/^{238}\text{U}$ age determinations that differ by less than 1σ (averaged), form a sub-population between 210 and 215 Ma (average ~213 Ma). We interpret this as the maximum depositional age of the sample, consistent with the ~208 Ma age for the base of the Voght determined previously (Mihalynuk et al., 2015). All other zircons analyzed have ages consistent with local derivation from the Nicola arc, including the sub-population of the three oldest grains at ~236 Ma.

3.2.2.3. Sample MMI14-15-13 (D11), Nicola Group Eastern belt, fine siliciclastic unit, ≤ 214 Ma, possibly <208 or even <202 Ma

Sample MMI14-15-13 was collected along the far eastern boundary of the northern part of the study area from the Eastern belt sedimentary rocks. Here the succession is mainly well-bedded turbiditic siltstone and argillite with lesser coarse wacke (see Mihalynuk et al., 2015). A carbonate-cemented arkose bed with a minimum thickness of ~15 cm was sampled (Fig. 25).



Fig. 25. U-Pb sample MMI14-15-13 of a light-weathering, coarse-grained arkose bed that is carbonate cemented (between the clipboard and hammer).

Sixty-two zircons analyzed yield a probability distribution peak at ~214 Ma (Fig. 26); however, if we use the same multigrain population reliability criteria as for Sample GMC14-50-2 (2σ less than 5% of the zircon age determination, and with $^{207}\text{Pb}/^{235}\text{U}$ and $^{206}\text{Pb}/^{238}\text{U}$ age determinations that differ by less than 1σ), then a 208 Ma subpopulation can be identified, but so too can a two-grain population with an average age of 202 Ma and very similar Pb, Th and U isotopic compositions (Friedman et al., 2016). This 202 Ma $^{206}\text{Pb}/^{238}\text{U}$ determination pair may provide the youngest reliable maximum depositional age. Either way, the strata are clearly too young to underlie the Nicola arc and must instead represent deposition coeval with arc growth. All zircons analyzed have ages that are consistent with derivation from the Nicola arc, with the oldest grains around 230 Ma. No grains from an old continental source were detected.

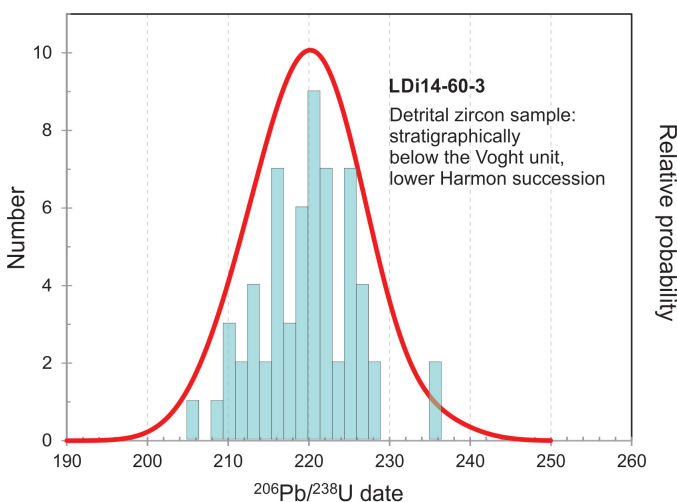


Fig. 24. Histogram of LA-ICPMS age determinations from individual detrital zircons from sample LDI14-60-3. Superimposed red curve is the cumulative age distribution showing resolved populations and their relative probabilities as determined by the ISOPLOT software of Ludwig (2003).

3.2.2.4. Sample MMI14-62-1 (D14), post-Nicola Group conglomerate near Shea Lake, ≤ 190 Ma, probably <185 Ma

Sample MMI14-62-1 was collected from a sandstone layer in a section of oxidized reddish brown conglomerate outcrop about 3 km west of Shea Lake (Figs. 2, 27). Analyses of 62 grains (Fig. 28) indicate a peak at in the probability density distribution of ~190 Ma (maximum depositional age) and ~215 Ma (age of most common source). A subpopulation of four grains with tightest errors of run at ~185 Ma may provide a younger maximum depositional age. A conspicuous lack of zircons between ~201 and ~197 Ma is consistent with the lack of known magmatism in the region during this period.

In the northwest part of the study area, a polymictic, maroon conglomerate unconformably overlies Late Triassic limestone (Hendriks unit) and is overlain by interbedded maroon epiclastic sandstone and bladed feldspar porphyry flows of the Voght unit (>202 Ma; see above). Mihalynuk et al. (2015) referred to this conglomerate as the 'Shea conglomerate' and included it in the upper part of the Nicola Group. However, at the western edge

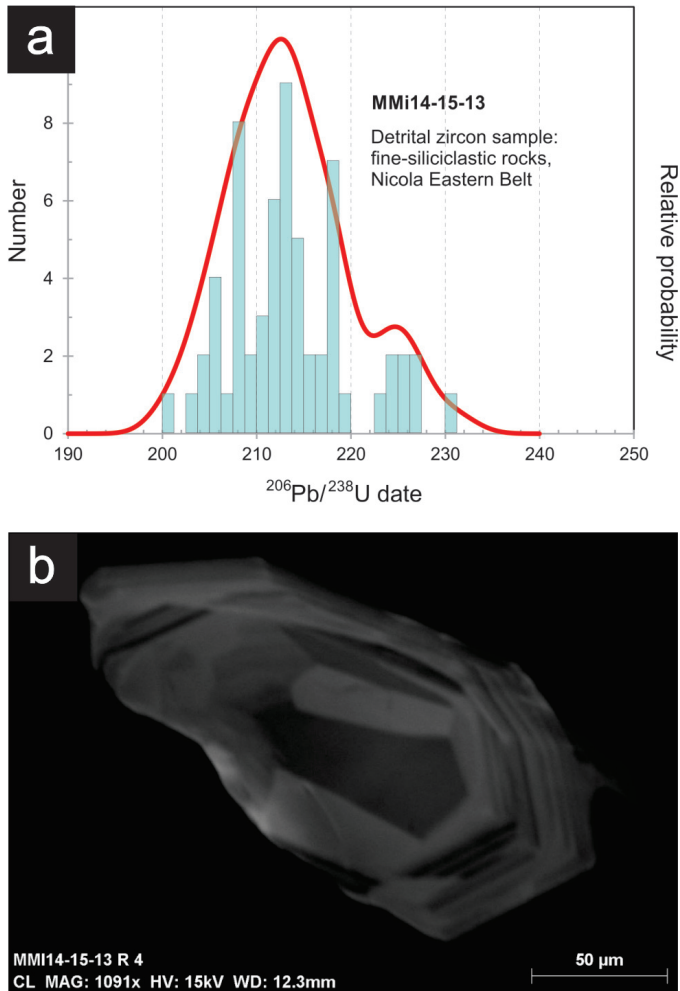


Fig. 26. a) Histogram of LA-ICPMS age determinations for individual detrital zircons from sample MMI14-15-13. Superimposed red curve is the cumulative age distribution showing resolved populations (~214 and ~225 Ma) and their relative probabilities as determined by the ISOPLOT software of Ludwig (2003). However, a younger age is possible, based upon an average of the two youngest grains that have nearly identical U, Pb, and Th compositions (Friedman et al., 2016). **b)** Image of cathodoluminescence of the largest of the two young grains, a broken euhedral crystal.

of the study area similar conglomerates appear to sit above the Nicola Group (unit Kc in Diakow and Barrios, 2008; unit Ks in Monger, 1989) and, as indicated by the detrital zircon ages above, the conglomerates near Shea Lake are younger than ~190 Ma. We now restrict use of the name ‘Shea conglomerate’ to the conglomerate near Shea Lake, which contains a higher proportion and greater diversity of plutonic clasts, and includes siliceous clasts resembling chert (Diakow and Barrios, 2008). ‘Harmon conglomerate’ is used to refer to the older Nicola Group conglomerate, which contains rhyolite and limestone as major clast types.



Fig. 27. Oxidized reddish brown, massive sandstone interbedded in conglomerate near Shea Lake.

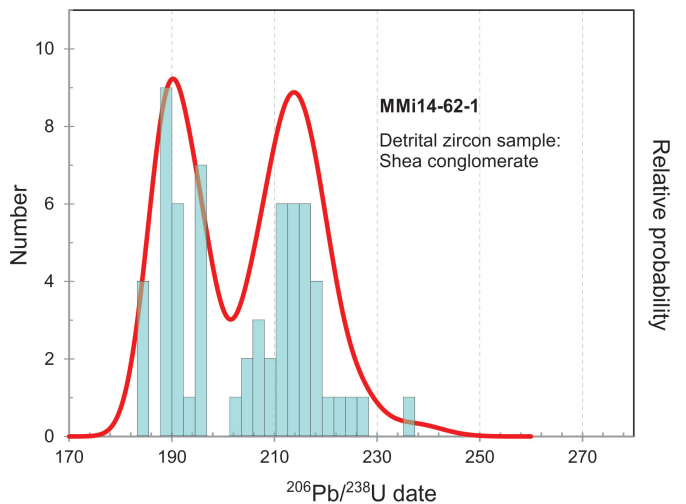


Fig. 28. Histogram of LA-ICPMS age determinations from individual detrital zircons from sample MMI14-62-1. Superimposed red curve is the cumulative age distribution showing resolved populations and their relative probabilities as determined by the ISOPLOT software of Ludwig (2003).

3.2.2.5. Sample GMC14-60-2 (D15), post-Nicola Group Bates chert pebble conglomerate; <163 Ma possibly <134 Ma

The Bates unit, comprising tabular beds of granule to boulder conglomerate, with abundant well-rounded black chert clasts, is at least 420 m thick, and forms a belt west of Aspen Grove that extends for about 17 km (Fig. 2; Mihalynuk et al., 2015). Clasts of lithologies other than black chert are significant only in northern exposures (Mihalynuk et al., 2015). Sample GMC14-60-2 was collected from a chert granule to pebble-rich bed of

the Bates conglomerate, uncharacteristically fine-grained for the cobble and boulder-rich conglomerate (Fig. 2). Geological constraints on the age of the conglomerate are based on its unconformable relationship with youngest dated Nicola strata (<201 Ma Tillery unit) near the northern margin of Allison pluton. Farther south, the Spences Bridge Group (104 Ma; Early Cretaceous) is deposited on the Allison pluton without any intervening Bates conglomerate. If Bates conglomerate was deposited and then eroded prior to the sub-104 Ma unconformity, the geologically-constrained conglomerate age would be between ~201, and 104 Ma.

A total of 65 grains were analyzed, resulting in a multi-peaked spectrum with a main population at 163 Ma, and multi-grain subpopulations at 153, 188, 210, 240 and, perhaps, at 305 Ma (Fig. 29a). Two old grains were analyzed: 1400 and 2750 Ma (Friedman et al., 2016). Both $^{207}\text{Pb}/^{235}\text{U}$ and the more reliable $^{206}\text{Pb}/^{238}\text{U}$ determinations on the youngest grain (Fig. 29b)

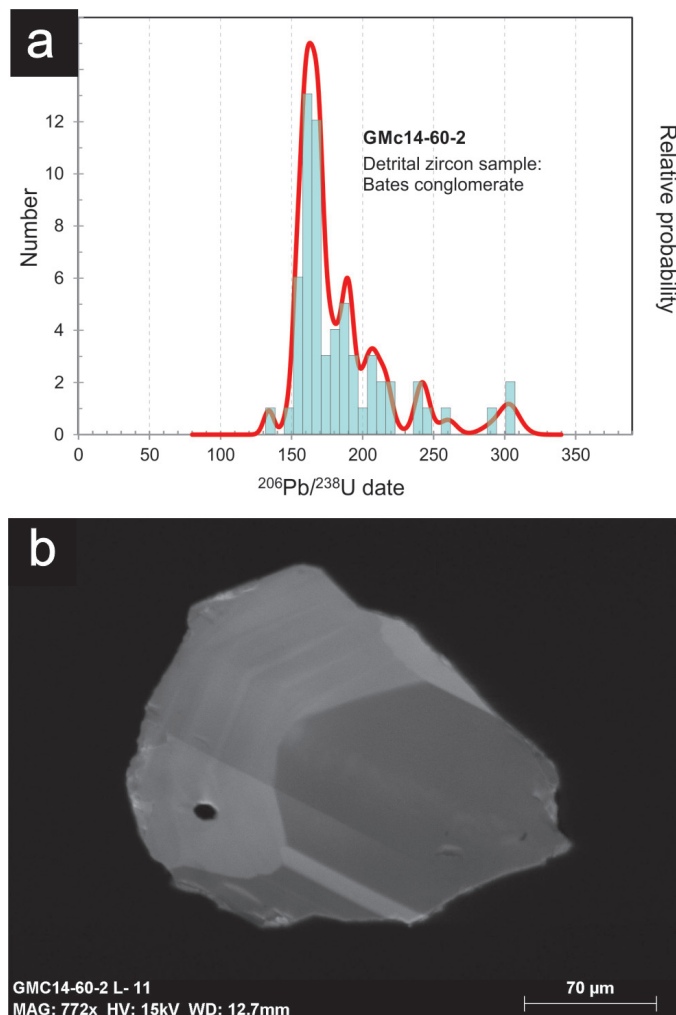


Fig. 29. a) Sample GMC14-60-2, Bates conglomerate zircon age spectra. Not shown are two Precambrian grains with $^{207}\text{Pb}/^{235}\text{U}$ ages of 1400 ± 36 Ma and 2753 ± 53 Ma. **b)** Cathodoluminescence image of the youngest grain. It yielded coeval $^{207}\text{Pb}/^{235}\text{U}$ and $^{206}\text{Pb}/^{238}\text{U}$ ages of 134 ± 15 Ma and 134 ± 7.3 Ma (2σ errors).

suggest ages 134 ± 15 Ma and 134 ± 7.3 Ma (2σ errors). Accepting the age of this single zircon would support assigning the Bates unit to unit Ks of Monger (1989; Early Cretaceous); if the age is spurious then main 163 Ma population peak would confirm assigning the conglomerate to unit 9 of Preto (1979; Late Jurassic).

The main 163 Ma detrital zircon population peak coincides with the age of the Osprey batholith and the newly defined Osprey volcanic unit (sample MMI14-59-12, 163.2 ± 0.2 Ma; see above), the closest occurrences of which are now 19 km away. Given the paucity of clasts other than black chert, the 163 Ma zircons may represent air fall material derived from Osprey-related volcanism. The Triassic zircon populations are readily explained by derivation from Nicola arc lithologies (see discussion of other TIMS ages above and Mihalynuk et al., 2015). However, no source of chert is known in the region between the Osprey batholith and the Bates conglomerate, and the sparse latest Carboniferous and single Mesoproterozoic and Archean grains require distant external sources.

4. Discussion: Implications for southern Nicola arc evolution

Acknowledged challenges to our understanding of the Nicola arc have historically been poor exposure and incomplete preservation, but probably even more problematic has been the lack of tight geochronological control. To address this problem, the SNAP objectives were rooted in establishing a better geochronological framework. A significant body of new age data are presented here, and implications of these data can be regional in scope.

Late Carnian to late Norian were previously thought to be the interval for Nicola arc development (Late Triassic; Schau, 1968; Preto, 1979), but arc development can now be shown to extend from latest Middle Triassic (Ladinian) to latest Late Triassic (Rhaetian). Moreover, distinctive stratigraphic units, dated isotopically or by fossils, demonstrate Early Norian stratigraphic links across the Western and Central belts proposed by Preto (1979) and that, by the Rhaetian, the arc was mainly eroding, as recorded by volcano-sedimentary lithofacies that extend continuously eastward from Central into the Eastern belt.

4.1. Proximity of Nicola arc to North America

The Nicola arc was constructed on a variety of basement rocks mainly of island arc character, the oldest with Late Silurian fossils (Read and Okulitch, 1977). However, the underpinnings of the Quesnel terrane have long-been debated with some workers arguing that North American crust extends unbroken beneath the Nicola arc (e.g., Erdmer et al., 2002; Thompson et al., 2006). Lack of Precambrian detrital zircons from analyses of samples reported here and in previous reports on the southern Nicola arc (Mihalynuk et al., 2014; Mihalynuk et al., 2015) support geographic separation from North America through the Triassic. Not one of the detrital zircons in the Triassic samples examined is older than Carboniferous, and the first appearance of Precambrian zircons is in post-Nicola

rocks (Bates conglomerate, Late Jurassic-Early Cretaceous). While not a conclusive test, lack of Precambrian zircons is inconsistent with the idea that craton underpins the Nicola arc. Yet just to the north of the study area, in the Nicola Horst, clasts up to 1038 Ma are reported (Erdmer et al., 2001, 2002; Moore, 2000; Moore et al., 2000), demonstrating that Precambrian domains may have existed beneath the Nicola arc, at least as local crustal fragments.

4.2. Nicola arc flares to life in the Middle Triassic

Rhyolite lava and fragmental rocks, with pillowed basalts, mark initial volcanic activity in the Nicola arc (238.15 \pm 0.33 Ma, sample MMI13-30-4 in Mihalynuk et al., 2015; 238.6 \pm 0.3 Ma, sample MMI15-55-13, this paper), that produced the rhyolite-rich epiclastic unit yielding a population of detrital zircons at \sim 239 Ma (sample MMI14-23-15; see Fig. 22). These rocks extend across the Central belt, scattered for 30 km between Coalmont and Missezula Mountain. They represent a pulse of nascent submarine arc magmatism. A similar age for arc initiation in northern Stikinia is recorded by the Joe Mountain volcanic rocks in Yukon (Hart, 1997; Piercey, 2004) which are Ladinian (242-235 Ma timescale of Ikeda and Tada, 2014), supporting a link between Stikinia and Quesnellia by that time (e.g., Mihalynuk et al., 1994). Inception of calc-alkalic porphyry-style mineralization by \sim 229 Ma in northern Stikinia (Mihalynuk et al., this volume) suggests that the Stikine arc was sufficiently thick to form porphyry deposits by late Middle Triassic.

In the northern part of the Nicola arc near Quesnel Lake, conodonts extracted from the base of the volcanic unit are early to middle Anisian (Struik, 1988). Nicola arc initiation could, therefore, be even older than recorded herein (see Fig. 7). It is possible that further dating will push the age of southern Nicola arc initiation to older ages.

4.3. Nicola arc growth

Following the early rhyolitic event (\sim 239 Ma), accelerated arc growth is reflected in a heterogeneous accumulation of plagioclase-augite phyric basalt and andesite lava and fragmental rocks interstratified with subordinate epiclastic rocks that are found throughout much of the Central and Western belts. The initial age of this volcanic episode has not been established. However, conodonts from a limestone-bearing conglomerate sampled in the Central belt (site TN10-1, Monger, 1989, GSC collection C88062; M.J. Orchard, p. comm, 2015) and a reassessment of conodont collections in the Geological Survey of Canada archive, indicate that carbonate sedimentation in the study area started near the Carnian-Norian boundary (\sim 227 Ma chronostratigraphic chart of Cohen et al., 2013, updated 2015). Multiple carbonate beds in the marker interval, which are interspersed with felsic tuffs throughout the Western belt, extend without tuffs into the Central belt. The age of the marker interval (224-223 Ma) is well established by conodont and U-Pb TIMS data (Fig. 7). The age data also confirm continuity between Western and Central belt units, and

establish earliest emergence of parts of the Nicola arc to photic depths in the Carnian and likely subaerial exposure by mid-Early Norian (Fig. 7).

Carbonate deposition marks a period of reef construction supporting a rich fauna (Schau, 1968) in shoaling sectors of the emergent Nicola arc. The style of volcanism also changed during carbonate sedimentation, with the introduction of rhyolite and dacite flows and fragmental rocks that provide the first evidence of subaerial eruptions. At times, phreatic eruptions produced ash-clouds charged with water vapor giving rise to accretionary lapilli tuff, and small-volume welded ash-flow tuffs, and rhyolite flows. Interbedding of subaqueous (fossil-bearing limestone; exhalative chert beds) and subaerial (welded rhyolite tuffs) deposits in the marker interval at Castillion Creek (224.58 \pm 0.22 Ma) provides evidence for frequent changes in relative sea level.

Because of the restricted range of isotopic ages and the relatively small volume of felsic rocks preserved in the Western belt marker interval, the duration of felsic volcanic activity is thought to be brief. However, a broader time span of volcanic activity is suspected from the substantial volume of mafic and intermediate volcanic and epiclastic rocks with thin accretionary lapilli tuff beds above the marker interval at Castillion Creek (estimate of 1100 to 1300 m exposed at Selish Mountain). The intrusive contact of the Coldwater pluton and thermal aureole developed adjacent to this section indicates that volcanism ceased by \sim 210 Ma.

4.4. Early Norian cross-arc correlation

Identical middle-Early Norian limestones, confirmed mainly by conodont fauna and few ammonoids (M.J. Orchard, 2016, unpublished fossil report; and fossil identifications in Preto, 1979), are now demonstrated to extend across the northwestern structural boundary between Western and central belts. However, generally interspersed felsic rocks have not been found with exposures of Hendriks limestone in the Central belt, adjacent to Kane Valley (Mihalynuk et al., 2015). Here the apparent absence of these distinctive quartz-bearing tuffs is tentatively attributed to removal during uplift and erosion affecting part of the up-thrown Central belt.

4.5. Deformation of Nicola arc preceding Cu-Au porphyry epoch

Evidence of a Late Triassic collision is widespread throughout Quesnellia and Stikinia (e.g., Logan and Mihalynuk, 2014). In the study area, it is manifested by thrusts and conglomeratic redbed deposition and concomitant changes in the arc chemistry, from predominantly basaltic to pulses of alkalic basalt and high-silica andesite (apatite-biotite-quartz-phyric) volcanoclastic strata (\sim 202.3 \pm 0.3 Ma, MMI14-62-4) with copper mineralization (Logan and Mihalynuk, 2014). Deformation led to uplift of the Central belt in the Norian and erosion to the level of Hendriks limestone (middle-Early Norian). Erosion apparently obliterated the entire record of pre-210 Ma volcanic strata that are still preserved throughout the

Western belt. Evidence of this erosion is recorded by locally thick, oxidized polymictic conglomerates in the Harmon succession that contain felsic volcanic and limestone clasts, both probably derived from the distinctive early Norian marker strata (~223 to 224 Ma), and abundant granitic clasts that potentially signal exhumation and erosion of the nearby Allison pluton (~223 Ma, sample MMI14-50-2, this paper) and older country rocks.

Deformation leading to uplift and erosion occurred after ~215 Ma, based on the age of the youngest dated rocks that are incised, and probably between ~208 Ma and ~201 +0.31/-0.4 Ma when arc aggradation resumed. The latter ages are based on the youngest detrital zircons (conglomerate sample 12JLO51-47 in Mihalynuk et al. 2015; sandstone sample LDi12-60-3, this study) and age of a crosscutting dike (sample MMI13-16-3 in Mihalynuk et al., 2015).

East-vergent thrust faults, best displayed along highway roadcuts in the study area (Mihalynuk et al., 2015), may provide some indication of the duration of collision because they apparently cut Shrimpton unit strata in the Eastern belt, presumably derived from the ~202 Ma arc. Latest Triassic detrital zircons recovered from arkosic strata of the Eastern belt suggest a link between quartz-phyric eruptions from the Zig area in the Central belt. This connection is strengthened if the youngest two-grain population of Eastern belt sample MMI14-15-13 at 202 Ma (mean) is a depositional age recording direct pyroclastic fallout sedimentation or resedimentation of material immediately reworked from Zig tuffs, (202.3 ±0.3 Ma, sample MMI14-5-62-4). Projected along-strike to the north, these thrusts should be cut by the undeformed ~193 Ma Pennask batholith (sample MMI14-19-3; see also Mihalynuk et al., 2015 and Fig. 2). Extensive overburden obscures any such relationship; although no thrust faults or folds have been recognized within the Pennask batholith.

More regionally, this deformation may be manifested in the Mount Lytton complex, about 50 km to the west, where strongly deformed quartzo-feldspathic gneiss is cut by a locally foliated granodiorite. U-Pb ages from these units are 225 ±5 and 212 ±1 Ma (Parrish and Monger, 1992), suggesting that onset of deformation is possibly older than in the study area.

4.6. Nicola arc wasting

The late arc history is recorded in strata previously described as part of the Eastern belt, which spans more than 20 km across the northern part of the study area (Figs. 2, 3). Rocks of the Central belt (Fairweather unit) extend eastward into mainly clastic and lesser volcanic components of the Eastern belt (Shrimpton, Paradise, Eastern fine siliciclastic units) speculated to represent lateral facies equivalents (Mihalynuk, et al., 2015). Magmatic activity appears to have waned as the Nicola arc was dissected to the level of epizonal plutons, with detritus transported to the arc flanks. Coarse conglomerate of the Fairweather unit, mostly on the eastern flank of the arc, is composed of subequal proportions of massive basaltic flows and, oxidized volcanic breccia and conglomeratic deposits. To

the east, the Shrimpton is generally finer grained and better stratified, with sandstones that contain marine fauna in rare limey layers, monzonite-clast conglomerate, and generally thinner mafic flow deposits, including thin (<1m to several m) alkaline basalt flows. Farther east, the Paradise unit is mainly volcanic and pluton clast-bearing conglomerate (commonly with pyroxene- and hornblende-bearing clasts), and flows. Mafic flow deposits comprise local thick accumulations within conglomerate. Farthest east, and not in contact with other facies, are parallel bedded, interstratified siltstone and minor mudstone, presumed to represent deposition in relatively deep marine waters.

Detrital zircon geochronology supports this correlation if the youngest zircon subpopulation (~202 Ma; sample MMI14-15-13) represents the depositional age of the Eastern fine siliciclastic unit. If so, it is coeval with the Fairweather unit, which was dated previously as ~201-202 Ma based on detrital zircons from maroon tuffaceous siltstone, and U-Pb TIMS from a cross-cutting dike (samples MMI13-16-6, Mihalynuk, et al., 2015).

The youngest absolute ages for magmatism in the Nicola arc are from the ~201 Ma dike (sample MMI13-16-3, Mihalynuk et al., 2015) cutting the Fairweather unit, and andesites from Zig unit (Mihalynuk et al., 2015), which has a U-Pb TIMS age of ~202 Ma (sample MMI14-62-4). These rocks may represent terminal volcanism in the Nicola arc. Diagnostic phenocrysts from high-silica andesitic fragmental rocks at Zig, that include quartz, biotite, and fine- to medium-grained apatite prisms, were incorporated in the Shrimpton unit, probably due to dispersal as components of air-borne ash falls. Analcime basalts, localized in the Fairweather and Shrimpton units as relatively thin flows, represent a distinctive alkaline volcanic pulse late in the arc's history, confirming stratigraphic continuity between units.

4.7. Early Jurassic (late Pliensbachian) deformation

A second stage of deformation may be recorded by the <190 Ma (possibly ~185 Ma) Shea conglomerate. No folding, faulting or fabrics can be directly attributed to this event. It is possible that many of the 25 detrital zircons (of the 62 analyzed) that overlap the age of the 193.11 ±0.16 Ma Pennask batholith (see MMI14-19-3) were derived from this or a coeval volcano-intrusive complex. If the age is correct, the Shea conglomerate may be regionally important; its depositional age corresponding with the age of Quesnel docking in the south (e.g., Parrish and Wheeler, 1983, Archibald et al., 1983; Murphy et al., 1995; Colpron et al., 1996) and north (e.g., Nixon et al., 1995) and development of a regional unconformity in both Quesnellia and Stikinia (e.g., Nelson and Bellefontane, 1996; Brown et al., 1996; Hart, 1997; and see summary in Logan and Mihalynuk, 2014). In the Ashcroft area to the west, carbonaceous marine shale and lesser sandstone of the Lower Jurassic Ashcroft Formation strata were overthrust by Nicola Group rocks around this same time (Travers, 1978).

4.8. Source of black chert clasts in Bates conglomerate?

The source of the chert clasts in the Bates conglomerate remains a mystery. Perhaps chert-rich pelagic deposits of the oceanic Cache Creek terrane were thrust over the Nicola arc, like in northern British Columbia, where Cache Creek overthrust Stikinia during final collision of Stikinia (Monger and Ross, 1971; Ricketts et al., 1992) as it rotated into alignment with the Quesnellian backstop (Mihalynuk et al., 1994). In northern British Columbia, this event is well dated as Middle Jurassic ~173 Ma (Mihalynuk et al., 2004), but a northern hinge produces a geometric constraint requiring collision at the southern latitude of the Nicola Arc during later times. In the south, early-middle Callovian chert deposition (based on radiolarian data; Cordey and Schiarizza, 1993) requires that Stikinia-Quesnellia docking, if it even occurred at the latitude of Merritt, did not happen until after ~165 Ma (2015 IUGS time scale, Cohen et al., 2013). Such timing is consistent with the main age distribution peak at 163 Ma (Fig. 29) and possible derivation from coeval Osprey volcanism (163.2 ± 0.2 Ma, sample MM14-59-12), and Osprey batholith (~162-166 Ma) rocks. To the immediate north, in the Nicola Horst, north of Nicola Lake (Fig. 2), rhyodacite and felsic porphyry clasts of 157 and 161 Ma may be part of a correlative conglomerate (Erdmer et al., 2002). Here the Nicola Group is structurally removed and the conglomerate lies above the Bob Lake assemblage, which contains clasts of 1.04 Ga felsic metaporphry and is cut by 230 and 219 Ma tonalite and diorite (Erdmer et al., 2002).

4.9. Early Cretaceous deformation

Two pulses of Early Cretaceous deformation are recognized regionally, but in the study area no structures can be conclusively related to the older pulse. In the Vernon area to the immediate east, the oldest pulse is represented by intense deformation fabrics in the 162 Ma Kalamalka shear zone that overprint 171 Ma orthogneiss (Glombick et al., 2006). Immediately southwest of the study area, are east vergent thrusts (with a dextral component) and late syn-kinematic tonalite gneisses of the Eagle Complex (157 ± 4 Ma), and Zoa complex volcanic strata that are cut by a possibly comagmatic quartz diorite (153 ± 10 Ma; U-Pb zircon, Greig et al., 1992).

A younger pulse of Early Cretaceous deformation is manifested in the study area by west-vergent thrust imbrication of the Bates conglomerate with Nicola arc strata. If the youngest reliable detrital zircon age in the Bates conglomerate is 134 Ma, as argued above, then deformation is bracketed between 134 and 104 Ma, the younger age constraint provided by the largely undeformed Spences Bridge Group (Diakow and Barrios, 2008), although west of the study area, the Spences Bridge is deformed within the Nicoamen syncline (Monger, 1985). This deformation may be related to interaction between the Insular and Intermontane superterrane between 135 Ma and the oldest probable stratigraphic link at 130 Ma (Umhoefer and Schiarizza, 1996). Further study of the Bates conglomerate, testing for youngest detrital zircons, and extracting radiolaria

from its clasts are required before concrete conclusions can be drawn.

5. Conclusions

Thanks to an ever-expanding network of logging roads and a growing geochronological dataset not available to earlier workers, a more detailed picture of Nicola arc evolution is emerging. Nicola arc construction began by ~239 Ma as recorded by regional felsic pulse of magmatism. Ensuing arc aggradation was mainly by accumulation of mafic, pyroxene and pyroxene-hornblende-phyric volcanic flows and flow breccia as recorded in the Central belt. Felsic volcanic strata were important at ~224 Ma. Well preserved in the Western belt, felsic strata were likely more important regionally, but were removed in other areas by erosion during terrane collision and uplift at ~210 Ma. Strata were deposited on the broad unconformity surface after ~208 Ma (upper part of the Harmon succession), but magmatism seemed to wane until termination of Nicola arc volcanism at ~202 Ma. Copper-gold porphyry-style mineralization was emplaced during the collision and uplift, and early waning magmatic arc stages, when arc wasting predominated and thick coarse clastic deposits formed to the east. Shortening of the arc, attributed to the ~210 Ma and later deformation, is in evidence as folds and thrust faults, including thrust imbrication of Late Jurassic or Early Cretaceous chert pebble conglomerate with Nicola arc strata. Nicola Arc construction, destruction, and deformation are coeval with those in other arc segments within Quesnel and Stikine terranes providing further bases for correlation and prediction of porphyry mineralization along the length of British Columbia.

Acknowledgments

We are indebted to past workers in the southern Nicola arc, especially J.W.H. Monger and V.A. Preto, both of whom have generously shared their time and knowledge with us in the field. Fieldwork in 2013 and 2014 benefitted from the diligent work of G. McEwan and M. Henderson, and in 2015 by T. Findley. Reviews by P. Schiarizza and L. Aspler, neither of whom agree with all of our interpretations, significantly improved this contribution.

References cited

- Archibald, D.A., Glover, J.K., Price, R.A., Farrar, E. and Carmichael, D.M., 1983. Geochronology and tectonic implications of magmatism and metamorphism, southern Kootenay arc and neighbouring regions, southeastern British Columbia, Part 1: Jurassic to mid-Cretaceous. *Canadian Journal of Earth Sciences*, 20, 1891-1913.
- Armstrong, R.L. and Petö, P., 1981. Eocene quartz-feldspar porphyry intrusions west of Okanagan Lake, southern B.C.: K-Ar dates and Sr isotopic composition. *Northwest Geology*, 10, 13-19.
- Ash, C.H., Reynolds, P.H., Creaser, R.A. and Mihalynuk, M.G., 2007. $^{40}\text{Ar}/^{39}\text{Ar}$ and Re-O Isotopic Ages for hydrothermal alteration and related mineralization at the Highland Valley Cu-Mo deposit (NTS 092I), southwestern British Columbia; In: *Geological Fieldwork 2006*, British Columbia Ministry of Energy Mines and Petroleum Resources, British Columbia Geological Survey Paper 2007-1, 19-24.

- Breitsprecher, K. and Mortensen, J.K., 2004. BC Age 2004A-1: A database of isotopic age determinations for rock units from British Columbia; British Columbia Ministry of Energy, Mines and Petroleum Resources, British Columbia Geological Survey Open File 2004-03.
- Cohen, K.M., Finney, S.C., Gibbard, P.L., Fan, J.-X., 2013; updated. The ICS International Chronostratigraphic Chart. *Episodes* 36, 199–204.
- Cordey, F. and Schiarizza, P., 1993. Long-lived Panthalassic remnant; the Bridge River accretionary complex, Canadian Cordillera. *Geology*, 21, 263–266.
- Crowley, J.L., Schoene, B. and Bowring, S.A. 2007. U-Pb dating of zircon in the Bishop Tuff at the millennial scale. *Geology*, 35, 1123–1126.
- Diakow, L.J. and Barrios, A., 2008. Geology and mineral occurrences of the mid-Cretaceous Spences Bridge Group near Merritt, southern British Columbia (Parts of NTS 092H/14, 15, 092I/02, 03). In: *Geological Fieldwork 2008*, British Columbia Geological Survey, British Columbia Ministry of Energy Mines Petroleum Resources Paper 2009–1, 63–80.
- Duke, E.F., Redden, J.A. and Papike, J.J., 1988. Calamity Peak layered granite-pegmatite complex, Black Hills, South Dakota: part 1. Structure and emplacement. *Geological Society America Bulletin*, 100, 825–840.
- Erdmer, P., Heaman, L., Creaser, R.A., Thompson, R.I. and Daughtry, K.L., 2001. Eocambrian granite clasts in southern British Columbia shed light on Cordilleran hinterland crust. *Canadian Journal of Earth Sciences*, 38, 1007–1016.
- Erdmer, P., Moore, J.M., Heaman, L., Thompson, R.I., Daughtry, K.L. and Creaser, R.A., 2002. Extending the ancient margin outboard in the Canadian Cordillera: record of Proterozoic crust and Paleocene regional metamorphism in the Nicola Horst, southern British Columbia. *Canadian Journal of Earth Science*, 39, 1605–1623.
- Friedman, R.M., Mihalynuk, M.G., Diakow, L.J. and Gabites, J.E., 2016. Southern Nicola Arc Project 2015: Geochronologic data constraining Nicola Arc history along a transect near 50°N. British Columbia Ministry of Energy and Mines, British Columbia Geological Survey, Geofile 2016-3.
- Gerstenberger, H. and Haase, G. 1997. A highly effective emitter substance for mass spectrometric Pb isotopic ratio determinations. *Chemical Geology*, 136, 309–312.
- Glombick, P., Thompson, R.I., Erdmer, P., Heaman, L., Friedman, R.M., Villeneuve, M., Daughtry, K.L., 2006. U-Pb constraints on the thermotectonic evolution of the Vernon Antiform and the age of the Aberdeen gneiss complex, southeastern Canadian Cordillera. *Canadian Journal of Earth Sciences*, 43, 213–244. doi:10.1139/E05-096.
- Greig, C.J., Armstrong, R.L., Harakal, J.E., Runkle, D., van der Heyden, P., 1992. Geochronometry of the Eagle Plutonic Complex and the Coquihalla area, southwestern British Columbia. *Canadian Journal of Earth Sciences*, 29, 812–829.
- Groves, E.W., 1989. Geological report and work proposal on the Siwash Creek Property. In: British Columbia Ministry of Energy, Mines and Petroleum Resources, Assessment Report 19472.
- Hunt, P.A. and Roddick, J.C., 1990. A compilation of K-Ar ages: Report 19. In: *Radiogenic Age and Isotopic Studies, Report 3*. Geological Survey of Canada Paper 89-02, 153–190.
- Ickert, R.B., Thorkelson, D.J., Marshall, D.D. and Ullrich, T.D., 2009. Eocene adakitic volcanism in southern British Columbia: Remelting of arc basalt above a slab window. *Tectonophysics*, 464, 164–185.
- Ikeda, M., and Tada, R., 2014. A 70 million year astronomical time scale for the deep-sea bedded chert sequence (Inuyama, Japan): Implications for Triassic–Jurassic geochronology. *Earth and Planetary Science Letters*, 399, 30–43.
- Jaffey, A.H., Flynn, K.F., Glendenin, L.E., Bentley, W.C. and Essling, A.M., 1971. Precision measurement of half-lives and specific activities of ²³⁵U and ²³⁸U. *Physics Review*, C4, 1889–1906.
- Lefebvre, D.V., 1976. Geology of the Nicola Group in the Fairweather Hills, British Columbia. M.Sc. Thesis, Queen's University, 179p.
- Logan, J.M. and Mihalynuk, M.G., 2014. Tectonic controls on early Mesozoic paired alkaline porphyry deposit belts (Cu-Au ±Ag-Pt-Pd-Mo) within the Canadian Cordillera. *Economic Geology*, 109, 827–858.
- Logan, J.M., Mihalynuk, M.G., Ullrich, T., and Friedman, R.M., 2007. U-Pb ages of intrusive rocks and ⁴⁰Ar/³⁹Ar plateau ages of copper-gold-silver mineralization associated with alkaline intrusive centres at Mount Polley and the Iron Mask batholith, southern and central British Columbia. In: *Geological Fieldwork 2006*, British Columbia Ministry of Energy, Mines and Petroleum Resources, British Columbia Geological Survey Paper 2007-1, 93–116.
- Long, D.G., 2015. Provenance and depositional framework of braided and meandering gravel-bed river deposits and associated coal deposits in active intermontane piggyback basins: The Upper Jurassic to Lower Cretaceous Tantalus Formation, Yukon. Yukon Geological Survey, Open File 2015-23.
- Ludwig, K.R., 2003. Isoplot 3.09: a geochronological toolkit for Microsoft Excel. Berkeley Geochronology Center, Special Publication 4, Berkeley.
- Massey, N.W.D., MacIntyre, D.G., Desjardins, P.J., Cooney, R.T., 2005. Geology of British Columbia (whole province digital map), British Columbia Ministry of Energy, Mines and Petroleum Resources, British Columbia Geological Survey Geofile 2005-1.
- Massey, N.W.D., Gabites, J.E., Mortensen, J.K., 2012. LA-ICP-MS geochronology of the Greenwood gabbro, Knob Hill complex, southern Okanagan, British Columbia. *Geol. Fieldwork 2013–1*.
- Mattinson, J.M., 2005. Zircon U-Pb chemical abrasion (CA-TIMS) method: combined annealing and multi-step partial dissolution analysis for improved precision and accuracy of zircon ages. *Chemical Geology*, 220, 47–66.
- Mihalynuk, M.G. and Logan, J.M., 2013a. Geological setting of Late Triassic Cu-Au porphyry mineralization at the Dillard Creek property near Merritt. In: *Geological Fieldwork 2012*, British Columbia Ministry of Energy and Mines, British Columbia Geological Survey Paper 2013-1, 97–114.
- Mihalynuk, M.G. and Logan, J.M., 2013b. Geological setting of Late Triassic Cu-Au porphyry mineralization at Miner Mountain, Princeton southern British Columbia. In: *Geological Fieldwork 2012*, British Columbia Ministry of Energy and Mines, British Columbia Geological Survey Paper 2013-1, 81–96.
- Mihalynuk, M.G., Nelson, J. and Diakow, L.J., 1994. Cache Creek Terrane entrapment: oroclinal paradox within the Canadian Cordillera. *Tectonics*, 13, 575–595.
- Mihalynuk, M.G., P. Erdmer, Ghent, E.D., Cordey, F., Archibald, D.A., Friedman, R.M., Johannson, G.G., 2004. Coherent French Range blueschist: Subduction to exhumation in < 2.5 m.y.? *Geological Society of America Bulletin*, 116, 910–922. doi:10.1130/b25393
- Mihalynuk, M.G., Logan, J.M., Friedman, R.M. and Preto, V.A., 2010. Age of mineralization and “Mine Dykes” at Copper Mountain alkaline copper-gold-silver porphyry deposit (NTS 092H/07), south-central British Columbia. In: *Geological Fieldwork 2009*, British Columbia Ministry of Energy and Mines, British Columbia Geological Survey Paper 2010-1, 163–171.
- Mihalynuk, M.G., Logan, J.M., Diakow, L.J., Friedman, R.M. and Gabites, J., 2014a. Southern Nicola Arc Project (SNAP): preliminary results. In: *Geological Fieldwork 2013*, British Columbia Ministry of Energy and Mines, British Columbia Geological Survey Paper 2014-1, 29–57.
- Mihalynuk, M.G., Friedman, R.M., Gabites, J.E. and Logan, J.M., 2014b. Southern Nicola Arc Project 2013: Geochronological data. British Columbia Ministry of Energy and Mines, British Columbia

- Geological Survey, GeoFile 2014-3.
- Mihalynuk, M.G., Diakow, L.J., Logan, J.M. and Friedman, R.M., 2015. Preliminary geology of the Shrimpton Creek area (NTS 092H/15E, 16W) Southern Nicola Arc Project. In: Geological Fieldwork 2014, British Columbia Ministry of Energy and Mines, British Columbia Geological Survey Paper 2015-1, 129–163.
- Monger, J.W.H., 1977. Upper Paleozoic rocks of northwestern British Columbia. Geological Survey of Canada, Paper , pp. 255-262.
- Monger, J.W.H. 1985. Structural Evolution of the Southwestern Intermontane Belt, Ashcroft and Hope Map Areas, B.C.. In: Current Research, Part A, Geological Survey of Canada, Report 85-1A, 349-358.
- Monger, J.W.H., 1989. Geology, Hope, British Columbia. Geological Survey of Canada, Map 41-1989.
- Monger, J.W.H. and Ross, C.A. 1971. Distribution of fusilinaceans in Western Canadian Cordillera. Canadian Journal of Earth Sciences, 8, 259-278.
- Monger, J.W.H., Souther, J.G., Gabrielse, H., 1972. Evolution of the Canadian Cordillera; a plate-tectonic model. American Journal of Science, 272, 577–602.
- Moore, J.M., 2000. Nicola Horst, southern British Columbia: window into the pre-Triassic margin of North America? In: Current Research, Geological Survey of Canada, Paper 2000-A16, 6p.
- Moore, J.M., Gabites, J.E., Friedman, R.M., 2000. Nicola horst: toward a geochronology and cooling history. In: Slave–Northern Cordillera Lithospheric Evolution (SNORCLE) Transect and Cordilleran Tectonics Workshop Meeting, pp. 25–27, f^o http://wmsmir.cits.mcan.gc.ca/index.html/pub/geott/ess_pubs/211/211139/cr_2000_a16.pdf, accessed December, 2015.
- Mundil, R., Ludwig, L.R., Metcalfe, I. and Renne, P.R., 2004. Age and timing of the Permian mass extinctions: U/Pb dating of closed system zircons. Science, 305, 1760-1763.
- Murphy, D.C., van der Heyden, P., Parrish, R.R., Klepacki, D.W., McMillan, W., Struik, L.C. and Gabites, J., 1995. New geochronological constraints on Jurassic deformation of the western edge of North America, southeastern Canadian Cordillera. In: Jurassic Magmatism and Tectonics of the North American Cordillera, Geological Society of America, Special Paper 299, 159–171.
- Nelson, J.L., and Bellefontaine, K.A., 1996. The geology and mineral deposits of north-central Quesnellia; Tezzeron Lake to Discovery Creek, central British Columbia. British Columbia Ministry of Energy, Mines and Petroleum Resources, British Columbia Geological Survey Bulletin 99, 112p.
- Nixon, G.T., Archibald, D.A. and Heaman, L.M., 1993. ⁴⁰Ar–³⁹Ar and U–Pb geochronometry of the Polaris Alaskan-type complex, British Columbia; precise timing of Quesnellia–North America interaction. In: Geological Association of Canada / Mineralogical Association of Canada; Annual Meeting, Program with Abstracts, p. 76.
- Parrish, R.R. and Wheeler, J.O., 1983. A U–Pb zircon age from the Kuskanax Batholith, southeastern British Columbia. Canadian Journal of Earth Sciences, 20, 1751-1756.
- Parrish, R.R. and Monger, J.W.H., 1992. New U–Pb dates from southwestern British Columbia. Radiogenic Age Isotopic Studies, Geological Survey of Canada, Report 5, 87–108.
- Paterson, S.R., Vernon, R.H. and Tobisch, O.T., 1989. A review of criteria for the identification of magmatic and tectonic foliations in granitoids. Journal of Structural Geology, 11, 349–363.
- Patton, C., Hellstrom, J., Paul, B., Woodhead, J. and Hergt, J., 2011. Iolite: freeware for the visualization and processing of mass spectrometry data. Journal of Analytical Atomic Spectroscopy, 26, 2508-2518.
- Piercey, S.J., 2004. Reconnaissance geological and geochemical studies of the Joe Mountain Formation, Joe Mountain region (NTS 105D/15), Yukon. In: Yukon Exploration and Geology, 213–226.
- Preto, V.A., 1972. Geology of Copper Mountain. British Columbia Department of Mines and Petroleum Resources, Bulletin 59, 95 p.
- Preto, V.A. 1979. Geology of the Nicola Group between Merritt and Princeton: British Columbia Ministry of Energy, Mines and Petroleum Resources, British Columbia Geological Survey, Bulletin 69, 90p.
- Ray, G.E. and Dawson, G.L., 1994. The geology and mineral deposits of the Hedley gold skarn district, southern British Columbia. British Columbia Ministry of Energy, Mines and Petroleum Resources, Bulletin 87, 156p.
- Read, P.B. and Okulitch, A.V., 1977. The Triassic unconformity of south-central British Columbia. Canadian Journal of Earth Sciences, 14, 606-638.
- Renne, P.R., Swisher, C.C., III, Deino, A.L., Karner, D.B., Owens, T. and DePaolo, D.J., 1998. Intercalibration of standards, absolute ages and uncertainties in ⁴⁰Ar/³⁹Ar dating. Chemical Geology, 145, No. 1-2, 117-152.
- Ricketts, B.D., Evenchick, C.A., Anderson, R.G., and Murphy, D.C., 1992. Bowser Basin, northern British Columbia; constraints on the timing of initial subsidence and Stikinia–North America Terrane interactions. Geology, 20, 1119–1122.
- Schau, M.P. 1968. Geology of the Upper Triassic Nicola Group in south central British Columbia. Ph.D. Thesis, The University of British Columbia, Vancouver, Canada, 211p.
- Schiarizza, P., 2014. Geological setting of the Granite Mountain batholith, host to the Gibraltar porphyry Cu–Mo deposit, south-central British Columbia. In: Geological Fieldwork 2013, British Columbia Ministry of Energy and Mines, British Columbia Geological Survey Paper 2014-1, 95-110.
- Schiarizza, P., 2015. Geological setting of the Granite Mountain batholith, south-central British Columbia. In: Geological Fieldwork 2014, British Columbia Ministry of Energy and Mines, British Columbia Geological Survey Paper 2015-1, 19-39.
- Schmitz, M.D. and Schoene, B., 2007. Derivation of isotope ratios, errors, and error correlations for U–Pb geochronology using ²⁰⁵Pb–²³⁵U(²³³U)-spiked isotope dilution thermal ionization mass spectrometric data. Geochemistry, Geophysics, Geosystems, 8, Q08006. doi:10.1029/2006GC001492.
- Scoates, J.S. and Friedman, R.M., 2008. Precise age of the plantiferous Merensky Reef, Bushveld Complex, South Africa, by the U–Pb ID–TIMS chemical abrasion technique, Economic Geology, 103, 465-471
- Slama, J., Kosler, J., Condon, D.J., Crowley, J.L., Gerdes, A., Hanchar, J.M., Horstwood, M.S.A., Morris, G.A., Nasdala, L., Norberg, N., Schaltegger, U., Xchoene, B., Tubrett, M.N. and Whitehouse, M. J., 2007. Plesovice zircon – A new natural reference material for U–Pb and Hf isotopic microanalysis. Chemical Geology, 249, 1-35.
- Struik, L.C., 1988. Regional imbrication within Quesnel Terrane, central British Columbia, as suggested by conodont ages. Canadian Journal of Earth Sciences, 25, 1608-1617.
- Tafti, R., Mortensen, J.K., Lang, J.R., Rebagliati, M. and Oliver, J.L., 2009. Jurassic U–Pb and Re–Os ages for newly discovered Xietongmen Cu–Au porphyry district, Tibet: implications for metallogenic epochs in the southern Gangdese Belt. Economic Geology, 104, 127-136.
- Thirlwall, M.F. 2000. Inter-laboratory and other errors in Pb isotope analyses investigated using a ²⁰⁷Pb–²⁰⁴Pb double spike. Chemical Geology, 163, 299-322.
- Thompson, R.I., Glombick, P., Erdmer, P., Heaman, L.M., Lemieux, Y., Daughtry, K.L., 2006. Evolution of the ancestral Pacific margin, southern Canadian Cordillera: insights from new geologic maps. In: Paleozoic Evolution and Metallogeny of Pericratonic Terranes at the Ancestral Pacific Margin of North America, Canadian and Alaskan Cordillera, M. Colpron and J.L. Nelson (editors), Geological Association of Canada, Special Paper 45, pp. 433–482.

- Thorkelson, D.J. and Rouse, G.E., 1989. Revised stratigraphic nomenclature and age determinations for mid-Cretaceous volcanic rocks in southwestern British Columbia. *Canadian Journal of Earth Sciences*, 26, 2016-2031.
- Thorkelson, D.J. and Smith, A.D., 1989. Arc and intraplate volcanism in the Spences Bridge Group: implications for Cretaceous tectonics in the Canadian Cordillera. *Geology*, 17, 1093–1096.
- Travers, W.B., 1978. Overturned Nicola and Ashcroft strata and their relation to the Cache Creek Group, southwestern Intermontane Belt, British Columbia. *Canadian Journal of Earth Sciences*, 15, 99-116.
- Umhoefer, P.J., Schiarizza, P., 1996. Latest Cretaceous to early Tertiary dextral strike-slip faulting on the southeastern Yalakom fault system, southeastern Coast Belt, British Columbia. *Geological Society of America Bulletin*, 108, 768–785.
- Woodsworth, G.J., Anderson, R.G., Armstrong, R.L., Struik, L.C. and van der Heyden, P., 1992. Plutonic regimes. In: Gabrielse, H. and Yorath, C. J., (Eds.), *Geology of the Cordilleran Orogen in Canada*, 493–531.
- Wotzlaw, J.F., Guex, J., Bartolini, A., Gallet, Y., Krystyn, L., McRoberts, C.A., Taylor, D., Schoene, B. and Schaltegger, U., 2014. Towards accurate numerical calibration of the Late Triassic: High precision U-Pb geochronology constraints on the duration of the Rhaetian. *Geology*, doi:10.1130/G35612.1.

